Contents of issue 4 vol. LV

STABILITY CONSTRAINTS IN OPTIMIZATION OF CRACKED COLUMNS SUBJECTED TO COMPRESSIVE FOLLOWER LOAD

Sz. I m i e ł o w s k i, R. B o g a c z

Institute of Fundamental Technological Research
Polish Academy of Sciences
Świętokrzyska 21, 00-049 Warszawa, Poland

Maximization of the critical force of cracked columns, subjected to generalized follower force is discussed in the paper. The crack is assumed to be formed according to the opening and sliding modes and is modeled by a localized loss of stiffness. Influence of the crack stiffness and its localization on the value of the critical force is analyzed. The optimization process is based on the multimodal approach. The localization of crack with the critical force of the system equal to $137.17 \ EJ/L^2$ is found.

1. INTRODUCTION

The structure considered in the paper is loaded by a follower force, i.e. the force that moves with the body on which it acts and that preserves the same attitude to this body during the loading process. In the present model, the force inclination and its eccentricity are proportional to the actual structural displacements. The contact force between the rail and the wheel, the reaction force of the bridge span support, the force of the vapour pressure acting in the Laval rotor or friction force of fluid against the pipes in fluid conveying pipes, are examples of the considered loading in mechanical systems. Some of them are discussed in literature, see references in [1] and [2]. Stability and optimization of systems subjected to follower forces have been intensively developed for the last three decades, whereas new results introduce an improvement in the stability criteria and new research in optimization.

In literature, the optimization of nonconservative systems is often developed on example of a column subjected to a concentrated compressive follower load, tangential to the deflection curve. This simple structural model leads however to some difficulties in structural and numerical modeling. It is due to the fact that the system has no potential and is governed by non-selfadjoint differential equations. For example, differences of about 20% in the value of the critical force are obtained by the authors of [3] and [4], by using the same optimality criteria but different methods of solution: the variational one and FEM.

It is observed that the result of optimization of nonconservative systems de-
pends strongly on the starting point in the space of design variables, i.e. initial
dimensions of the column. The proper choice of initial parameters can be es-
sential for analysis. For example, a single crack located in the column span can
increase the value of critical force of the column or beam subjected to follower
compression [5, 14]. The optimal shape of a stepped column, shown in Fig. 1a,
was found by BOGACZ *et al.* [6]. Probably the first result in the class of contin-
uous variation of the column cross-sections was obtained by ŻYCZKOWSKI and
GAJEWSKI [7]. As far as the authors know, the best present result of the column
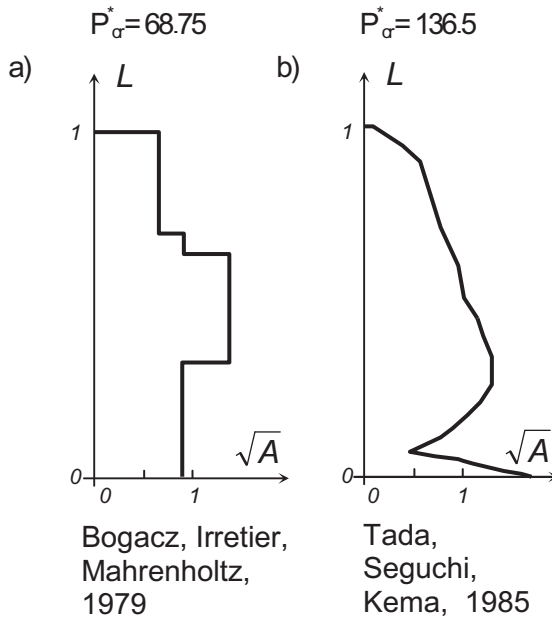shape optimization, shown in Fig. 1b, is reported by TADA *et al.* [8].

FIG. 1. Selected results of shape optimization of column subjected to follower compression.

In the present consideration the design variables, crack localization and stiff-
ness are searched through to find the maximum value of the critical force. Crack is
modeled by a localized loss of stiffness as an elastic joint with possible rotational
and shear deformation. The critical force is determined from the configuration
of characteristic curves on the force-frequency plane, which are obtained from
the characteristic equation of the problem. The flutter force, the local maximum
of characteristic curve graph, occurs at nonzero eigenfrequency, whereas buck-
ling occurs at the eigenfrequency equal to zero. In the multimodal analysis 4–6
first eigenfrequencies are considered. More details of the optimization process
are reported in Sec. 3.

2. FORMULATION OF THE PROBLEM

2.1. Model of the column

The considered model of column consists of segments of length l_i connected by elastic joints. The column is subjected to a generalized, follower compressive force P. The equation of motion for the i-th column segment, for small harmonic vibrations, has the form

$$(2.1) \qquad \frac{\partial^2}{\partial x^2}\left(EI_i\frac{\partial^2 y_i}{\partial x^2}\right) + P\frac{\partial^2 y_i}{\partial x^2} + \rho A_i \frac{\partial^2 y_i}{\partial t^2} = 0,$$

where ρA_i denotes the mass per unit length and EI_i – stiffness of the i-th segment. In the further analysis the cross-sections, masses and stiffnesses of the segments are assumed to be the same in the whole column. The separation of variables is considered in the form

$$(2.2) \qquad y_i(x,t) = w_i(x_i)\exp(i\omega t),$$

where ω is the angular frequency. The exact solution for the segment of uniform mass and stiffness distribution is given by

$$(2.3) \qquad w_i(x) = A_1\sinh\lambda_1 x_i + A_2\cosh\lambda_1 x_i + A_3\sin\lambda_2 x_i + A_4\cos\lambda_2 x_i,$$

where

$$(2.4) \qquad \lambda_{1/2} = \sqrt{\pm\frac{P}{2EI_i} + \sqrt{\left(\frac{P}{2EI_i}\right)^2 + \frac{\rho A_i\omega^2}{EI_i}}}.$$

2.2. Boundary conditions

The considered model of loading, the so-called generalized follower force, includes the variation of both the force horizontal displacement e and the force inclination at an angle of χ, as shown in Fig. 2a, [9]. These two parameters depend on both the actual generalized displacements, f and α, of the structure at the point of the force application. The bending moment $M = Pe$ and the transversal force component $H = P(\alpha - \chi)$ are finally included in the boundary conditions

$$(2.5) \qquad w(0,t) = 0, \qquad \frac{\partial}{\partial x}w(x_1,t)_{/x_1=0} = 0,$$

$$(2.6) \qquad \begin{aligned} &\frac{\partial^2}{\partial x^2}w(x_n,t)_{/x_n=L} + \lambda\left[\delta\frac{\partial}{\partial x}w(x_n,t) + \vartheta w(x_n,t)\right]_{x_n=L} = 0, \\ &\frac{\partial^3}{\partial x^3}w(x_n,t)_{/x_n=L} + \lambda\left[\mu\frac{\partial}{\partial x}w(x_n,t) + \gamma w(x_n,t)\right]_{x_n=L} = 0, \end{aligned}$$
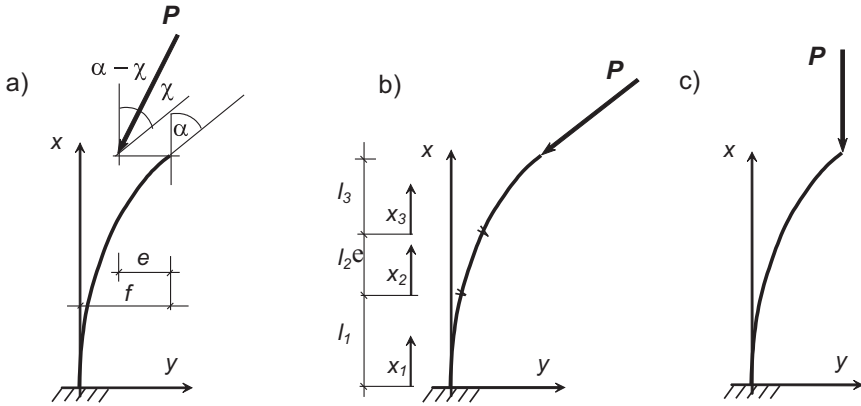
FIG. 2. a) Model of column subjected to generalized follower load,
b) Segmentation of the structure on example of Beck column,
c) Euler column.

where δ, ϑ, μ, γ are the non-dimensional parameters and L is the length of the column. In this way, values of the parameters δ, ϑ, μ, γ determine the boundary conditions.

Taking into account that the loading is an inseparable part of the whole system, the type of the boundary condition implies its conservativeness or non-conservativeness. Let us consider an operator F_x of the Eq. (2.1)

$$(2.7) \qquad F_x = \frac{\partial^2}{\partial x^2}\left(EI_i\frac{\partial^2 y_i}{\partial x^2}\right) + P\frac{\partial^2 y_i}{\partial x^2}.$$

The system is conservative if the operator (2.7) with respect to boundary conditions (2.5) and (2.6) is selfadjoint. E.g. for $e = 0$ and $\chi = \alpha$ ($\delta = \vartheta = \gamma = 0$, $\mu = 1$), the condition describes a conservative Euler column, shown in Fig. 2c, subjected to a force applied to the free end, the direction of which does not change during the loading process. For $e = 0$, $\chi = 0$ ($\delta = \vartheta = \gamma = \mu = 0$) the condition describes a nonconservative Beck column, shown in Fig. 2b, loaded by a force tangent to the column free end. This model will be considered in the following section.

2.3. Model of the crack

We assume that a crack was formed according to the opening mode and the sliding mode of development of the crack, so that in the mechanical model presence of the crack is expressed by a discontinuity in displacement and slope. Due to the fact that the column is loaded by a follower force, at location of the crack, $x = x_C$, the change of slope and shear depends on the rotary stiffness

χ_R as written in formula (2.8a), whereas the change of deflection and bending depends on the shear stiffness χ_S, as given in formula (2.8b):

(2.8a)
$$w_{i+1}^I(x_C) - w_i^I(x_C) = -\gamma_R w_{i+1}^{II}(x_C),$$

$$w_{i+1}^{III}(x_C) - w_i^{III}(x_C) = -\frac{P}{EJ}\gamma_R w_{i+1}^{II}(x_C),$$

(2.8b)
$$w_{i+1}(x_C) - w_i(x_C) = \gamma_S w_{i+1}^{III}(x_C),$$

$$w_{i+1}^{II}(x_C) - w_i^{II}(x_C) = \frac{P}{EJ}\gamma_S w_{i+1}^{III}(x_C).$$

where $(.)^I = d(.)/dx$ and $\gamma_R = 1/\chi_R$, $\gamma_S = 1/\chi_S$ represent additional flexibilities of the column due to the crack, which can be calculated on the basis of fracture mechanics. A model which is valid for a beam with a transverse open crack is discussed in [10, 11].

2.4. Segmentation of the structure and design variables

In what follows, the dimensionless quantities are used:

(2.9) $\quad \lambda^* = PL^2/EI, \qquad \omega^{*2} = \omega^2 \rho AL^4/EI, \qquad u_i = w_i/L, \qquad \varepsilon_i = x_i/L.$

The problem can now be rewritten in the following final form:

(2.10)
$$[u_i^{II}(\varepsilon_i)]^{II} + \lambda^* u_i^{II}(\varepsilon_i) - \omega^{*2} u_i(\varepsilon_i) = 0, \qquad 0 \le \varepsilon_i \le 1,$$

$$u_1(0) = u_1^I(0) = u_n^{II}(1) = [u_n^{II}(1)]^I = 0,$$

$$u_{i+1}^I(\varepsilon_C) - u_i^I(\varepsilon_C) = -\gamma_R^* u_{i+1}^{II}(\varepsilon_C),$$

$$u_{i+1}^{III}(\varepsilon_C) - u_i^{III}(\varepsilon_C) = -\frac{P}{EJ}\gamma_R^* u_{i+1}^{II}(\varepsilon_C),$$

$$u_{i+1}(\varepsilon_C) - u_i(\varepsilon_C) = \gamma_S^* u_{i+1}^{III}(\varepsilon_C),$$

$$u_{i+1}^{II}(\varepsilon_C) - u_i^{II}(\varepsilon_C) = \frac{P}{EJ}\gamma_S^* u_{i+1}^{III}(\varepsilon_C),$$

where $\gamma_i^* = \gamma_i EI/L$, $\chi_i^* = 1/\gamma_i^*$ are the dimensionless parameters of the joint flexibility and stiffness, respectively.

We look for the cracks localization ε_C and stiffnesses χ_R^*, χ_S^* which maximize the critical load under the following constraints: a constant total mass of the

column, a constant column cross-section A and the total column length L. For n cracks this condition is written as

$$(2.11) \qquad \sum_{i=1}^{n+1} l_i = 1,$$

where l_i is the length of the i-th column segment. For the localization of the crack at one of the column ends, $l_1 = 0$ or $l_{n+1} = 0$. The design variables of the problem are

$$(2.12) \qquad \Delta\alpha \in \{\varepsilon_C, \chi_R^*, \chi_S^*\}.$$

3. Optimality criteria based on multimodal analysis

Consider the optimization of a nonconservative Beck column under the constraints of dynamic stability. The objective function $\lambda_{cr}^* = \lambda_{cr}^*(\Delta\alpha)$, where $\Delta\alpha$ stands for a set of design variables, is not defined explicitly. The optimization conditions, imposed in the frequency domain, are defined as limitations on variation of the shape of characteristic curves. TADA *et al.* [12] proposed a definition of the optimal point as the one that represents the state for which all pairs of eigenvalues become double roots with the same value of critical forces, as shown in Fig. 3. In the present research it means that we should determine localization and stiffnesses of the joint, for which the successive double roots have equal values:

$$(3.1) \qquad \lambda_{12}^* = \lambda_{34}^* = \lambda_{56}^* = ...,$$

where λ_{ij}^* denotes the critical load corresponding to the i-th and j-th frequency branches in the force-frequency plane.
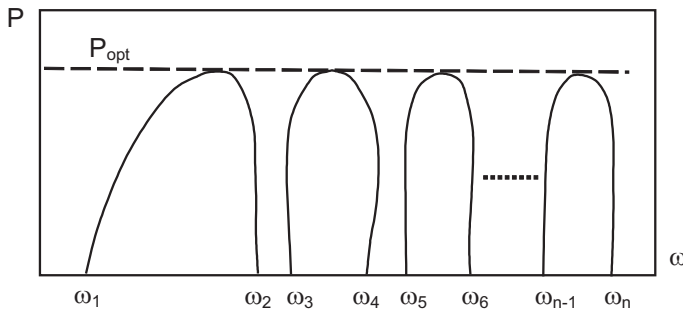

Fig. 3. Configuration of characteristic curves for the optimal shape.

The authors of [13] have noticed that for the developed cracks, flutter can occur with frequency tending to zero. Increasing of the joint stiffness produces

increasing of the flutter frequency. The condition of optimal structure can now be rewritten in the following form

$$(3.2) \qquad \lambda^*_{01} = \lambda^*_{23} = \lambda^*_{45} = \lambda^*_{67} = ...$$

The first term λ^*_{01} of formula (3.2) can be understood as flutter occurring with frequency tending to zero. Notice that this term can have a second meaning. With respect to divergent-flutter systems it can be understood as buckling for which the frequency is equal to zero.

In first optimizations the authors increased the value of λ^*_{12} like in [3] or $\lambda^*_{12} = \lambda^*_{34}$, similarly to [4]. In the analysis presented in [6] and [12] the first six eigenfrequencies were considered. Finally, we reduce the problem to increasing the value of λ^*_{opt} under the condition

$$(3.3) \qquad \lambda^*_{\text{opt}} \leq \lambda^*_{ij},$$

where $\lambda^*_{\text{opt}} = \lambda^*_{01}$, λ^*_{12} or λ^*_{23}.

Notice that the assumption (3.3) is very useful in calculations since the necessity of keeping the first two or three first values of the critical force within the range of acceptable accuracy can be eliminated.

The next constraint is introduced to preserve a high value of the critical force against the shape perturbation. Due to possible interactions between the successive characteristic curves, a discontinuous decrease in the critical force value can appear. The assumption of minimal distance between two successive characteristic curves prevents such interactions. The formula for a sufficient distance between two curves is as follows:

$$(3.4) \qquad \omega^*_{i+1} - \omega^*_i \geq c,$$

where c is a positive number and i denotes the i-th frequency branch. Such formulation of the condition was introduced in [12]. It is seen that a switch-over of characteristic curves resulting in determination of a critical force higher than λ^*_{opt} of formula (3.3) is permitted.

4. NUMERICAL EXAMPLES – MAXIMIZATION OF THE CRITICAL FORCE OF A CRACKED COLUMN

Let us consider the process of maximization of the critical force of a cracked column. The optimization process consists of two steps. In the first one, possible combinations of the design variables $\Delta\alpha_i$ are checked to find the values for which the critical force takes a higher value. In the second step, this result is taken as the initial guess for the gradient procedure. The procedure selects the

design parameter $\Delta\alpha$ by analyzing the configuration of characteristic curves and satisfying the conditions (3.2), (3.3) and (3.4). Notice that the condition (3.3) guarantees only a non-negative value of the gradient of the objective function and not the largest one. Discontinuous changes in the critical force are prevented by the condition (3.4). The obtained maximum value of the critical force is equal to $\lambda^*_{\text{cr}} = 137.17$ EI/L^2 for the crack localization of $\varepsilon_C = 0.382$ and stiffnesses $\chi^*_S = 0.01$ and $\chi^*_R = 0.0001$. The column is shown in Fig. 4a and the corresponding configuration of the characteristic curves is depicted in Fig. 4b. The value of the critical force is compared with the best result obtained for continuous mass distribution, reported by TADA et al. [8], shown in Fig. 1b.
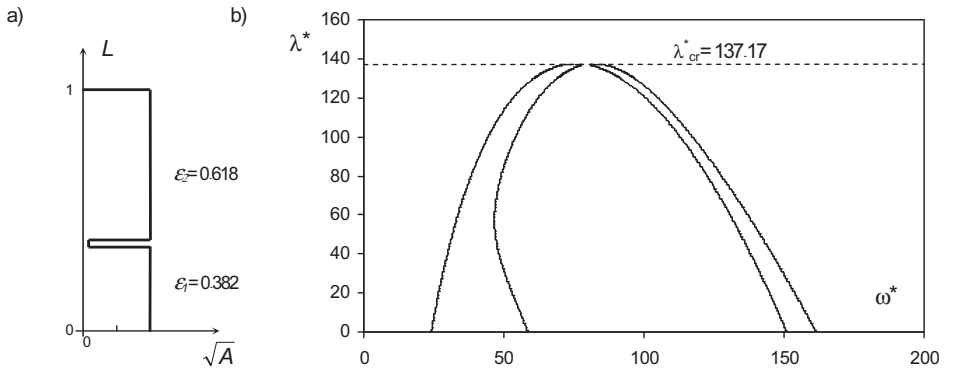

FIG. 4. Optimal localization of crack and respective shape of characteristic curves.

Notice that this result could be improved when higher frequencies would be taken into consideration. However, this requires greater computational efforts. On the other hand, due to a high sensitivity, such optimality is questionable from the viewpoint of the structure reliability and safety.

5. DISCUSSION OF STABILITY OF THE CRACKED COLUMNS AND CONCLUSIONS

The authors of [13] analyzed the problem of stability of column with localized loss of stiffness described by a model similar to that given by expression (2.8). On the force-frequency plane they observed two kinds of characteristic curves. One of them can be attributed to a column with a joint located at the fixed end, whereas the second kind concerns the column with a joint located at the free end. Notice that the second localization of the joint does not influence the stability of the column, the configuration of characteristic curves is the same as that for a uniform Beck column. By changing the position of the joint, the characteristic curves of one kind approach the origin of coordinates whereas the

curves of second kind move away from it. The same phenomenon is observed for the present model. In Fig. 5 the configurations of characteristic curves are shown on the example of a column with optimal localization of the crack, considered in the previous chapter. The curves of one kind are depicted by black line whereas the curves of the second kind – by a gray line.
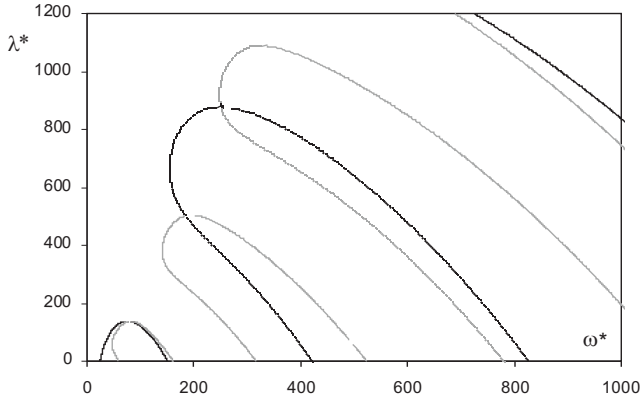

FIG. 5. Two kinds of eigencurves of column with optimal localization of crack.

An interesting observation concerns the stability of a column with crack which was formed according to the sliding mode, modeled by the loss of the shear stiffness, i.e. for $\chi_R^* \to \infty$ and arbitrary χ_S^*. Any localization of the joint and every value of the shear stiffness do not influence the stability of the system. For each joint location and its stiffness, the shape of characteristic curves and the value of critical force are the same as for a uniform column.

However, when the rotary stiffness of the crack is finite, the shear stiffness influences the shape of characteristic curves. An example is shown in Fig. 6,
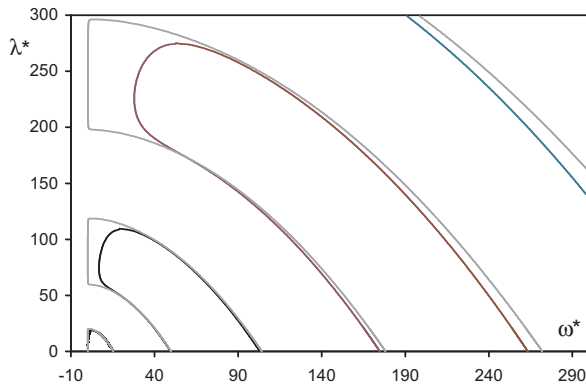

FIG. 6. Characteristic curves of column with crack placed at $\varepsilon_1 = 0.0$ for $\chi_R^* = 1e - 4$, $\chi_S^* \to \infty$ (gray) and $\chi_R^* = 1e\text{-}4$, $\chi_S^* = 1e4$ (black).

where the shape of characteristic curves for a joint of rotary stiffness $\chi_R^* = $ 1e-4 placed at $\varepsilon_C = 0.0$ and two different values of shear stiffness $\chi_S^* = $ 1e10 and $\chi_S^* = $ 1e4 are shown. It is seen that the column with hinge-joint, $\chi_S^* \to \infty$, loses stability by divergence. The successive critical forces occur with frequencies approximately equal to zero. Release of the shear flexibility causes that successive critical frequencies arise.

Let us consider the column with a crack which was formed according to the opening mode, modeled by the localized loss of the rotary stiffness, i.e. for $\chi_S^* \to \infty$ and arbitrary χ_R^*. The critical load versus dimensionless joint location ε_C is shown in Fig. 7. Notice that the critical load decreases considerably for $\varepsilon_C > 0.3$. Discontinuous changes of the critical force occur when the crack of $\chi_R^* = 0.1$ and $\chi_R^* = $ 1e-4 is located near the free end of the column. The discontinuities on the chart result from the qualitative changes of the shape of characteristic curves. The phenomenon is described e.g. in [5, 6] or [13].
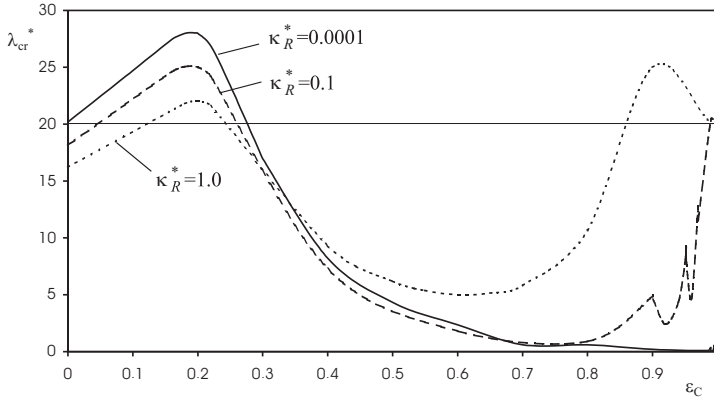

Fig. 7. Critical force versus hinge-joint localization for various joint stiffnesses.

Let us observe the shape of the curve plotted for the stiffness of $\chi_R^* = 1.0$. An analysis of this shape can give some information concerning optimal volume distribution of the column. The simplest way to increase the value of the critical force of the column of constant length and constant Young modulus, is to increase the moment of inertia, namely to enlarge the cross-sections of the column. We have concluded that the column cross-sections should be enlarged in these coordinates, for which the critical force is lower than that for a uniform column. On the other hand, the volume of the column can be taken away in these coordinates for which the critical force is higher than that for a uniform column. According to this, the optimal shape of the column relates directly to the shape of the curve plotted in Fig. 7.

In the modern mechanical systems the follower load can be caused e.g. by systems of active control. The present analysis shows that in the class of slender

columns subjected to follower load, the existence of a crack not always destroyed the structure. There are localizations of the crack, for which the critical force is higher than that of a uniform column. Designer can initialize such localization of the crack for which the cracked element under the action of the follower load will not be destroyed.

References

1. Sz. Imiełowski, *Modal forms of columns subjected to generalized follower force*, [in:] Theoretical Foundation of Civil Engineering, X Ukrainian-Polish Transaction, W. Szcześniak [Ed.], **10**, 141–150, 2002. 2.

2. Sz. Imiełowski, R. Bogacz, W. Kurnik, *Fixed point in frequency domain of structures subjected to generalized follower force*, Machine Dynamic Problems, **25**, 3/4, 169–182, 2001.

3. J. L. Claudon, *Characteristic curves and optimum design of two structures subjected to circulatory loads*, J. de Mecanique, **14**, 3, 531–543, 1975.

4. M. Hanaoka, K. Washizu, *Optimum design of Beck's column*, Computers and Structures, **ll**, 6, 473–480, 1980.

5. R. Bogacz, O. Mahrenholtz, *On stability of column under circulatory load*, Archives of Mechanics, **38**, 3, 281–287, 1986.

6. R. Bogacz, H. Irretier, O. Mahrenholtz, *Optimal design of structures under nonconservative forces with stability constraints*, Bracketing of eigenfrequencies of continuous structures. Proc. Euromech **112**, Budapest, Hungary, 43–65, 1979.

7. M. Życzkowski, A. Gajewski, *Optimal structural design*, Proc. IUTAM Symp. Non-Conservative Problems of Elastic Stability, Herrenhalb/Karlsruhe 1969, Springer Verlag, 295–30l, 1971.

8. Y. Tada, Y. Seguchi, K. Kema, *Shape determination of nonconservative structural systems by the inverse variational principle*. Memoirs of the Faculty of Engineering, Kobe University, **32**, 45–61, 1985.

9. M. Życzkowski, Stability of bars and bar structures, in: Strength of structural elements, M. Życzkowski [Ed.], 242–381, Elsevier, 1991.

10. W. M. Ostachowicz, M. Krawczuk, *Analysis of the effect of cracks on the natural frequencies of a cantilever beam*, Journal of Sound and Vibration (Academic Press), **150**, 2, 191–201, 1991.

11. M. Krawczuk, W. M. Ostachowicz, *Influence of cracks on dynamic stability of column*, Journal of Sound and Vibration (Academic Press), **167**, 3, 541–555, 1993.

12. Y. Tada, R. Matsurnoto, A. Oku, *Shape determination of nonconservative structural systems*, Proc. 1st Int. Conf. Computer Aided Optimum Design of Structures: Recent Advances, Southampton, 13–21, Springer, Berlin 1989.

13. R. Bogacz, Sz. Imiełowski, *Remarks on stability of discrete-continuous structure under circulatory load*, J. Theor. Appl. Mechanics, **4**, 32, 903–919, 1994.

14. Q. Wang, *A comprehensive stability analysis of a cracked beam subjected to follower compression*, Int. Journal of Solids and Structures, **41**, 4875–4888, 2004.

A GLOBAL OXIDATION SCHEME FOR PROPANE-AIR COMBUSTION SUITABLE FOR USE INTO COMPLEX REACTING FLOW COMPUTATIONS

P. K o u t m o s, G. G i a n n a k i s, P. M a r a z i o t i

**Department of Mechanical and Aeronautical Engineering
University of Patras**

Patras, Rio 26500, Greece

In Direct or Semi-Direct Numerical Simulations of turbulent reacting flows the exploitation of complex, realistic and detailed chemistry and transport models often results in prohibitive memory and CPU requirements when flows of practical relevance are treated.

The integrated Combustion Chemistry approach has recently been put forward as a methodology suitable for the integration of complex chemical kinetic and chemistry effects into large scale computational procedures for the calculation of complex and practical reacting flow configurations. Through this procedure, a reduced chemical kinetic scheme involving only a limited number of species and reactions is derived from a detailed chemical mechanism, so as to include major species and pollutants of interest in the main flow calculation. The chemical parameters employed in this integrated scheme i.e. rates, constants, exponents are then calibrated on the basis of a number of constraints and by comparing computations over a range of carefully selected laminar flames so as to match a number of prespecified flame properties such as adiabatic temperatures, selected target species profiles, flame speeds, extinction characteristics. The present work describes such an effort for a commonly used fuel of both the fundamental and practical importance that often is used to simulate the performance of higher hydrocarbons in practical engine simulations, i.e. propane. The proposed nine-step scheme involves nine major stable species and in addition to the basic propane oxidation model also includes NO_X production and soot formation submodels.

Key words: integrated Combustion Chemistry, reduced propane chemistry mechanisms, laminar flames, chemical reaction schemes.

NOTATIONS

A_k preexponential factor in the Arrhenius law of reaction k,
A_s particle surface area in soot model,
a strain rate ($\sec^{-1}$) in counterflow flames,
C_v constant in radiative flux expression,
c_p specific heat,
C_a constant in particle number density equation source term,
D, d diameter,
$D_{i-\mathrm{N2}}$ diffusion coefficient in binary mixture of the i-th species and nitrogen,
d_p carbon particle diameter in soot model source term,
E_{NOx} NOx emission index,
f_v soot volume fraction,

H	enthalpy,
H_i	enthalpy of species i,
h_i	absolute value of enthalpy,
h_{fi}^0	heat of formation at standard state,
I_{bik}	Planck function in radiative flux expression,
I_f	number of momentum equations solved,
k	specific reaction rate constant,
Le_i	Lewis number for species i,
M_s	molecular weight of soot,
M_i	molecular weight of species i,
N_s	number of species,
N_A	Avogadro number,
N_k	number of species involved in reaction k,
P_s	particle number density, in soot model,
P	static pressure,
q_r	radiative heat flux,
R_u	universal gas constant,
R1...9	number of reaction in reduced scheme,
R_{cyl}	radius in porous cylinder counterflow flame configuration,
r	radial direction,
S_L	laminar flame speed,
T	temperature,
u	axial velocity,
$u_{\mathrm{air},\infty}$	approach air velocity in porous cylinder counterflow flame configuration,
v	radial velocity,
v_w	fuel injection velocity in porous cylinder counterflow flame configuration,
X_i	mole fraction of species i,
Y_i	mass fraction of species i,
y	y axis, transverse direction,
z	z axis, axial direction,
w_i	net rate of production of species i.

GREEK SYMBOLS

α_k	temperature exponent in reaction step k,
Γ_Φ	transport coefficients in governing equations,
ζ_{ik}	intergration intensities in radiative flux expression,
$\eta_{c,\min}$	constant in particle number density equation source term,
λ	thermal conductivity,
$\nu'_{i,k},\ \nu''_{i,k}$	stoichiometric coefficients in forward and backward direction,
$\nu_{i,k}$	concentration exponents of species i involved in reaction k,
π	$3.14\ldots$,
ρ	density,
σ_B	Boltzmann constant,
$\Phi,\ \phi$	represents any variable (i.e. 1, u, v, H or Y_i) used in the governing equations,
[CxHy]	molar concentration of species i.

b	backward,
ex	extinction,
f	forward,
s	soot,
k	reaction step,
i	species i,
Nucl	nucleation,
Growth	growth.

1. Introduction

The combustion of hydrocarbons for the production of energy is a common and important phenomenon in many engineering applications. In most practical devices, chemical reactions usually take place within and strongly interact with a turbulent flow, and the adequate description of the combustion process requires the consideration of a large number of fluid and chemical parameters [1]. On the other hand, during the past decade the demand for higher efficiencies, the stringent emission regulations and the need to reduce costs in design and optimization procedures for combustion chambers, has prompted the exploitation of Computational Fluid Dynamics methods in support of experimental procedures [2–4].

Direct or Semi-Direct Numerical Simulations (e.g. DNS, LES) of turbulent reacting flows offer a promising tool toward understanding of the complex physics of these flows. The full potential and advantages of these techniques can best be realized when sufficiently complex and realistic but flexible and tractable chemistry and transport models are exploited [2, 5]. Currently, computational costs and numerical considerations preclude spatially three-dimensional turbulent simulations with detailed chemistry and transport models in the parameter range of practical interest. Instead, the judiciously reduced chemical mechanisms that can be employed profitably within DNS or LES and provide a realistic description of appropriate thermochemical parameters are preferred [2, 3, 6].

A number of methodologies have been exploited to simplify a detailed mechanism e.g. the systematic consideration of steady-state and partial equilibrium assumptions leading to skeletal mechanisms [7], the analysis and categorization of characteristic chemical time-scales of separate reaction groups [8] and the Integrated Combustion Chemistry (ICC) approach [9], which involves the use of a limited number of judiciously chosen species and reactions with kinetic parameters tuned to match a prespecified number of constraints and flame properties. The ICC approach, alone or in conjunction with other methodologies, offers a viable alternative systematic reduction procedure, targeting specific require-
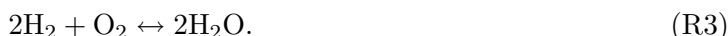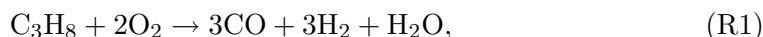
ments with reference both to the thermochemical submodels and to the complete computational procedure. In contrast to the first two approaches, [7, 8], it only involves a limited number of steps and focuses on major species and pollutants of interest for the main simulation, in the effort to avoid the burden of intermediate radicals and elementary rates altogether that would prohibitively burden the basic computational procedure.

The present work describes an effort along similar lines, to derive a simplified and tractable chemical scheme for the oxidation of propane, a fuel of practical interest, including NO_X and soot production models. Its chemical parameters are calibrated by using this scheme within one and two-dimensional reacting flow solvers and by computing a number of well documented one and two-dimensional and coflowing laminar flames, lifted and attached by matching a number of flame properties such as peak temperatures, major target species, flame speeds and extinction characteristics. The successful derivation and encouraging validation of the presently proposed scheme for propane lends support for an extension of the approach to more complex hydrocarbons, such as ethylene and alternative fuels of practical relevance such as H_2 and CH_3OH.

2. The integrated combustion chemistry methodology

2.1. The basic approach

The proposed approach is based on the requirement that the resulting mechanism must be able to predict, to a significant extent, what a state of the art multi-step reduced mechanism is predicting for one, two-dimensional and jet flames. The route to achieve this relies on the calibration of the rate parameters of a starting selected chemical scheme by computing laminar flames for which credible experimental data exist. In this investigation, the three-step reduced scheme given by KENNEL et al. [7] is chosen here as the starting mechanism for the basic methane oxidation:

$$C_3H_8 + 2O_2 \rightarrow 3CO + 3H_2 + H_2O, \tag{R1}$$

$$CO + H_2O \leftrightarrow CO_2 + H_2, \tag{R2}$$

$$2H_2 + O_2 \leftrightarrow 2H_2O. \tag{R3}$$

The original global rate parameters may be given in terms of linear combinations of many of the rates of the elementary reactions of the C_1-chain skeletal mechanism and may involve a number of intermediates and radicals (e.g. [7, 8, 10]). The original basic steps and species of (R1) to (R3) are retained but the target here is to produce global rates with simple kinetic parameters *exclud-*

ing altogether intermediate elementary rates and radicals in the resulting global rate expressions.

A framework to achieve this goal has been put forward by [9]. The *first* objective is prediction of the flame temperature and heat release in various cases. Because no extended product dissociation is allowed, the fuel heat of reaction is slightly (5%) reduced to reproduce the experimental temperatures. The *second* objective is the reproduction of variation of the laminar burning velocity versus mixture dilution as close as possible by regulating the pre-exponential constants (A_k), the activation energies (E_{Ak}) and the species exponents of the above three rates, to fit the available experimental data. An appropriate choice of a set of A_k, E_{Ak} and relevant exponents is additionally constrained by the adequate prediction of the extinction limits of selected opposed jet or stagnation point flames. The *third* objective is the adequate computation of targeted product species profiles for a range of strain rate values. This is interrelated with the requirement that the resulting scheme should be also capable of predicting unsteady effects, an aspect that represents the *fourth* objective and this is particularly significant in highly turbulent flame calculations and at conditions involving localized extinctions and reignitions. Here a strained counterflow flame configuration and a pulsating lifted-off coflow diffusion flame are used for such validation.

Apart from the choices for the chemistry model, the molecular transport model, can also affect the correct computation of the flame properties. As in massive complex flow simulations the simplified transport models are frequently exploited, (e.g. [2, 3, 6]), validation tests are here performed utilizing similar levels of complexity. Fick's law with constant Lewis numbers, Sunderland's law for viscocity, constant Prandtl and Schmidt numbers and temperature-dependent specific heats were presently employed. Only in the computations of the freely propagating 1-D premixed flames, diffusion coefficients in binary mixtures of the i-th species and N_2 were exploited.

Anticipating that radiative losses can have a significant influence on NO_X and soot levels, an optically thin radiation model was embodied in the calculations where it is assumed that the only significant radiating species are CO, CO_2, H_2O and soot. By employing an optically thin limit in which self-absorption of radiation is neglected, the divergence of the net radiative flux can be written as:

$$(2.1) \qquad \nabla q_r = C_V f_V T^5 + 4\pi \sum_{ik} \zeta_{ik} \rho_k I_{bik} \,,$$

where f_v is the soot volume fraction and I_{bik} is the Planck function evaluated at the gas band centers of the contributing vibration-rotation or pure rotational bands, whose integrated intensities are given by ζ_{ik}. The value of the

constant C_V is here taken as $4.243 \cdot 10^{-10}$, with units that give a power density in watts/cc with T in Kelvins, according to the suggestions of references [6, 10].

2.2. The proposed mechanism

The basic oxidation of propane is here conveniently represented by the aforementioned three-step scheme of reaction set (R1) to (R3). Regarding the production of NO_X it has been established that the three main routes to NO formation are the prompt, the thermal and the N_2O mechanism [2, 9, 11], while in rich environments the reburn mechanism is also known to be important. The N_2O production path here is not directly accounted for; its contribution however is indirectly apportioned through the calibration of the rate constants in the employed NOx scheme on the basis of experimental data that include the N_2O levels. The proposed scheme takes into account the remaining contributions through the set of reactions:

$$0.5N_2 + [O] \leftrightarrow NO, \tag{R4}$$

$$0\,C_3H_8 + N_2 + O_2 + 0[O] + 0H_2O \leftrightarrow 2NO + 0C_3H_8. \tag{R5}$$

The zero coefficients for C_3H_8, $[O]$ and H_2O in reaction (R5) mean that these species do not participate explicitly in this reaction but are included in the calibrated rate expressions. The required oxygen radical is here obtained from partial equilibrium assumptions [8, 11]. The involvement of water and oxygen radicals in the prompt production rate (e.g. Refs. [2, 11]) is therefore accounted for in the formulated reduced NOx reaction scheme. The influence of intermediates and radicals related to the fuel structure is necessarily mimicked through propane, which acts as a catalyst in reaction (R5).

To complete the overall scheme, a model for soot formation and oxidation has also been implemented employing many features from the successful soot model proposed by LINSTEDT [6, 10]. The underlying reactions for acetylene production are here all summed up and represented through one model reaction of the form:

$$2C_3H_8 \leftrightarrow 3C_2H_2 + 5H_2. \tag{R6}$$

The corresponding soot nucleation and growth processes are addressed following the modeling assumptions of reference [10] and represented as:

$$C_2H_2 \rightarrow 2C_s + H_2. \tag{R7}$$

The subsequent soot oxidation reactions due to OH radicals and O_2 is here modeled and expressed as:

$$C_s + 0.5O_2 \rightarrow CO, \tag{R8}$$

$$C_s + H_2O \rightarrow CO + H_2 . \tag{R9}$$

In line with the integrated concept of the proposed mechanism, the radicals involved in the original mechanism (e.g. OH, H) have been replaced by stable species (e.g. H_2O, H_2) addressed in the proposed reduced scheme. The resulting soot chemical scheme is implemented and applied by solving two additional transport equations for particle number density and soot mass fraction, as discussed below in Sec. 3.

2.3. Determination of global mechanism kinetic rate parameters

The first step in the calibration procedure involves the identification of an appropriate set of A_k and E_{Ak} values for the hydrocarbon chemistry starting from the aforementioned basic oxidation scheme (reactions (R1) to (R3)). An iterative approach is then employed aiming to adjust the kinetic rate parameters A_k, E_{Ak} and determine any species exponents with respect to the four target requirements described in Sec. 2.1. With the simple transport formulations described previously, the kinetic parameters are tuned and adjusted through a series of repeated test computations involving the prediction of the temperature and species profiles, the flame speed and the extinction behavior of laminar one and two-dimensional and coflowing jet flames within the context of the discussions of Sec. 2.2 and the constraints of Sec. 2.1. With the propane oxidation scheme established, the NO_X reactions ((R4) and (R5)) are then added. The appropriate initial set of A_k and E_{Ak} values is here chosen with guidance from and reference to several features of the relevant elementary NO_X production steps, (e.g. Ref. [9]). These rate parameters are then similarly tuned in repeated test computations in which close prediction of the NOx levels in 1-D freely propagating and 2-D coflow jet flame configurations is required.

The rate parameters of reaction (R4) are calibrated to achieve the correct prediction of thermal NO_X levels and then the prompt (Fenimore) and reburn contributions are apportioned through reactions (R5) in the test cases described in Sec. 4. In an analogous fashion the soot reaction scheme is finally added and the rate constants for reactions (R6) to (R9) are adjusted to reproduce the correct levels of C_2H_2 and soot volume fraction for the test cases selected and discussed below. The final set of the kinetic rate parameters is given in Table 1.

Table 1. Specific reaction rate constants for reduced C_3H_8-air oxidation scheme.

Rxn No.	Preexponential (A_k)	Temperature exponent, (a_k)	Activation energy, (E_{Ak})	Species exponents
1	3.5E5	1	12500	$C_3H_8^{0.6}$, $O_2^{1.0}$
2,f	48750	1.65	−300	$CO^{0.8}$, $H_2O^{1.25}$
2,b	$1.825*10^6$	1.14	−1000	$CO_2^{0.8}$, $H_2^{1.15}$
3,f	$4.2*10^8$	−0.72	0	$H_2^{1.15}$, $O_2^{0.65}$
3,b	$1.25*10^8$	−0.7	0	$H_2O^{1.25}$
4,f	$1*10^{10}$	0.3	37770	$[O]^{0.97}$
4,b	$7*10^7$	0.9	20600	$NO^{0.745}$, $[O]^{1.04}$
5,f	$1.5*10^{10}$	0	11100	$C_3H_8^{0.03}$, $N_2^{1.16}$, $O_2^{0.03}$, $H_2O^{0.5}$, $[O]^{1.0}$
5,b	$8*10^8$	0	8100	$C_3H_8^{0.05}$, $NO^{1.56}$
6,f	$5*10^{21}$	−4.35	25198	$C_3H_8^{0.92}$
6,b	$7.5*10^{19}$	−3.8	34500	$C_2H_2^{0.95}$, $H_2^{0.01}$
7	As reported in [10]	As reported in [10]	23000	$C_2H_2^{0.01}$
8	As reported in [10]	0.4	23850	As reported in [10]
9	3.6	0.75	0	$C_S^{0.1}$, $H_2O^{1.7}$

Units in mole/cm^3, sec^{-1}, K, cal/mole (species exponents not declared above are unity).

3. The numerical method

The flame configurations studied here are simulated by solving the time-dependent form of the two-dimensional gas-phase conservation equations for reacting flow. The adopted methodology is similar to that of [12] and closely derives from the formulations of [4]. Conservation equations for mass, momentum, energy and species are solved and the equation set can be expressed in e.g. cylindrical coordinates (z, r) with the general form:

$$(3.1) \quad \frac{\partial (\rho\phi)}{\partial t} + \frac{\partial (\rho u\phi)}{\partial z} + \frac{\partial (\rho v\phi)}{\partial r}$$

$$= \frac{\partial}{\partial z}\left(\Gamma_\phi \frac{\partial\phi}{\partial z}\right) + \frac{\partial}{\partial r}\left(\Gamma_\phi \frac{\partial\phi}{\partial r}\right) - \frac{\rho v\phi}{r} + \frac{\Gamma_\phi}{r}\frac{\partial\phi}{\partial r} + S_\phi$$

ρ, u and v denote density, axial and radial velocities and, depending on the variable used for Φ (i.e. 1, u, v, H or Y_i), this general form represents the conservation of either mass, momentum, energy or species. The transport coefficients

Γ_Φ are obtained from the molecular transport model discussed previously while the source terms, S_Φ, are provided in Table 2, and their treatment is similar to that discussed in [12]. The enthalpy H is defined as:

$$H = \int_{T_0}^{T} c_p \, dt = \sum_{1}^{N_s} Y_i H_i = \sum_{1}^{N_s} Y_i(h_i - h_{fi}^0),$$

where h and h_f^0 represent the enthalpy and the heat of formation at standard state respectively.

Table 2. Transport coefficients and source terms appearing in governing equations.

Equations	ϕ	Γ_ϕ	S_ϕ
Continuity	1	0	0
Axial momentum	u	μ	$-\dfrac{\partial p}{\partial z} + (\rho_0 - \rho)g + \dfrac{\partial}{\partial z}\left(\mu\dfrac{\partial u}{\partial z}\right) + \dfrac{\partial}{\partial r}\left(\mu\dfrac{\partial v}{\partial z}\right) + \dfrac{\mu}{r}\dfrac{\partial v}{\partial z}$ $-\dfrac{2}{3}\dfrac{\partial}{\partial z}\left(\mu\dfrac{\partial u}{\partial z}\right) + \dfrac{\partial}{\partial z}\left(\mu\dfrac{\partial v}{\partial r}\right) + \dfrac{\partial}{\partial z}\left(\mu\dfrac{v}{r}\right)$
Radial momentum	v	μ	$-\dfrac{\partial p}{\partial r} + \dfrac{\partial}{\partial z}\left(\mu\dfrac{\partial u}{\partial r}\right) + \dfrac{\partial}{\partial r}\left(\mu\dfrac{\partial v}{\partial r}\right) + \dfrac{\mu}{r}\dfrac{\partial v}{\partial r} - 2\mu\dfrac{v}{r^2}$ $-\dfrac{2}{3}\dfrac{\partial}{\partial r}\left(\mu\dfrac{\partial u}{\partial z}\right) + \dfrac{\partial}{\partial r}\left(\mu\dfrac{\partial v}{\partial r}\right) + \dfrac{\partial}{\partial r}\left(\mu\dfrac{v}{r}\right)$
Species mass fractions	Y_i	ρD_{i-N_2}	$\dot{w}_i$
Energy	H	$\dfrac{\lambda}{c_p}$	$\nabla\left[\dfrac{\lambda}{c_p}\sum_{1}^{N_s}\left(\mathrm{Le}_i^{-1} - 1\right)H_i\nabla Y_i\right] - \sum_{1}^{N_s} h_{fi}^0 \dot{w}_i$

Le_i is the Lewis number of species i, defined as $\mathrm{Le}_i = \lambda/\rho c_p D_{i-N2}$, where D_{i-N2} is the diffusion coefficient of the i-th species in a binary mixture of that species and nitrogen. These binary diffusion coefficients were exploited only in the computations of the freely propagating 1-D premixed flame configurations. Also the global species and the state equations,

$$(3.2) \qquad Y_{N_2} = 1.0 - \sum_{1}^{Ns-1} Y_i, \qquad P = \rho R_u T \sum_{1}^{N_s} \dfrac{Y_i}{M_i}$$

where R_u is the universal gas constant, T is the temperature, M_i is the molecular weight of species i, together with the net rate of production of the i-th species

due to the number of chemical reactions N_k expressed as:

$$(3.3) \qquad w_{i,k} = \left(\nu''_{i,k} - \nu'_{i,k}\right) * A_k * T^{a_k} \exp\left\{-\frac{E_{Ak}}{R_u T}\right\} \prod_{i=1}^{N_k} \left(\frac{\rho Y_i}{M_i}\right)^{\nu_{i,k}}$$

which appear in the source terms of the species conservation equations, complete
the set of governing equations. Here Y_i is the mass fraction of the species i, $\nu'_{i,k}$
and $\nu''_{i,k}$ are the stoichiometric coefficients of species i in reaction k in forward
and backward direction, $\nu_{i,k}$ are concentration exponents of species i involved in
reaction step k, A_k and E_{Ak} are the preexponential factor and activation energy
in the Arrhenius law of reaction k.

The computational domain in each different test case is commonly bounded
by inflow and outflow boundaries, wall and symmetry or axis planes. Constant
values of the variables were specified at inlet sections, with velocity, tempera-
ture and mixture compositions taken from the reported experiments. At lines of
symmetry the radial (normal) velocity was set to zero and a zero gradient was
assumed for the axial velocity, temperature and species concentrations. A zero
gradient was applied at the outflow boundaries that were carefully located far
away from regions of steep gradients of the variables. Open boundaries were im-
plemented as slip lines where a zero radial (normal) velocity and a zero gradient
condition for axial velocity, temperature and species concentrations were ap-
plied. The governing equations are integrated by using a finite-volume approach
with a staggered, non-uniform grid system. The momentum equations are dis-
cretized using an implicit QUICKEST finite-difference scheme (KOUTMOS *et al.*
[4]), while a hybrid scheme is employed for stability in the species equations. An
iterative alternating direction implicit (ADI) technique [12] is used for solving
the set of $N_s + I_f + 1$ algebraic equations ($N_s + 1$ is the number of species and
the enthalpy equation and I_f represents the number of the momentum equations
solved, depending on the dimensions of the configuration studied). A stable nu-
merical integration procedure is achieved by coupling the species and energy
equations through the chemical reaction source terms and the chemical source
terms are linearized to improve convergence. The pressure field is calculated at
every time step by solving the pressure Poisson equations in every grid node
simultaneously and exploiting the LU (Lower and Upper diagonal) matrix de-
composition technique. For the validation test runs involving freely propagating
premixed flame configurations, the standard PREMIX Sandia code [13] was used.
The extinction behavior of non-premixed stagnation point flames to steady and
unsteady strain rate were investigated by adapting the basic two-dimensional
detailed flow solver to the particular flame/geometry configuration.

The chemical reaction scheme for soot production and oxidation is combined
with the solution of two additional model transport equations for particle number
density, P_s, and soot mass fraction, Y_s, as proposed by [6]. These have the same

form as Eq. (3.1), written for the i-th species as given in Table 2. Chemical reaction (R7) represents here both nucleation and growth while reactions (R8) and (R9) represent the soot oxidation process.

The relevant source term, S_{Ys}, for soot mass fraction, Y_s, can then be written:

$$(3.4) \quad S_{Y_s} = 2k_{7,\text{Nucl}} \left[C_2 H_2 \right] M_s$$

$$+ 2k_{7,\text{Growth}} A_s \left[C_2 H_2 \right] M_s - k_8 A_s \left[O_2 \right] M_s - k_9 A_s \left[H_2 O \right] M_s$$

while that for particle number density, P_s, can be expressed as:

$$(3.5) \qquad S_{P_s} = 2k_{7,\text{Nucl}} \left[C_2 H_2 \right] \frac{N_A}{\eta_{C,\text{min}}} - 2C_a d_p^{1/2} \left(\frac{6\sigma_B T}{\rho_s} \right) (\rho P_S)^2 .$$

According to the recommendations of references [6, 10] the following set of constants is utilized in the above source expressions. M_s and ρ_s are the molecular weight and density of soot, $\sigma_B = 1.38 \cdot 10^{-23}$ J/K is the Boltzmann constant, $N_A = 6.022 \cdot 10^{26}$ particles/kmol is the Avogadro number, $C_a = 9$, $\eta_{c,\text{min}} = 60$ and $A_s = \pi d_p^2 \rho\, P_s$ is the particle surface area with $d_p = (6Y_s/\pi\rho_s P_s)$, the carbon particle diameter. Here the nucleation and growth rate constants used above, $k_{7,\text{Nucl}}$ and $k_{7,\text{Growth}}$ for reaction (R7), and the oxidation rate constant due to oxygen, k_8, are taken as suggested by [6, 10] with only minor changes as indicated in Table 1, while the rate constant, k_9, due to soot oxidation from OH is duly modified to take into account the replacement of the radical OH contribution in reaction R9 with the stable available species H_2O. The tuned reaction rate constants for reactions (R6) to (R9) are also given in Table 1.

4. Results and discussion

The performance of the basic oxidation mechanism was evaluated by computing unstretched laminar premixed propane-air flames having different equivalence ratios, Φ. An important validation parameter is the laminar flame speed, S_L, which was presently calculated and is compared against experimental data from the extended literature (e.g. references [2, 6, 7]) as a function of equivalence ratio Φ in Fig. 1a. The predicted lean and stoichiometric part of the S_L curve appears quite satisfactory with a peak S_L of 0.45 m/sec against experimental values in the region 0.39 to 0.47. The rich S_L branch however seems to be underpredicted possibly due to exclusion of intermediate radicals such as H and OH. In an initial effort to alleviate, in a simple manner, this rich branch deficiency and allow a more fruitful exploitation of the proposed scheme, a parameterization and tabulation of the preexponential factor of reaction (R3) as a simple function of the local equivalence ratio was attempted targeting the more correct prediction of the rich S_L branch values as depicted in Fig. 1a. A more
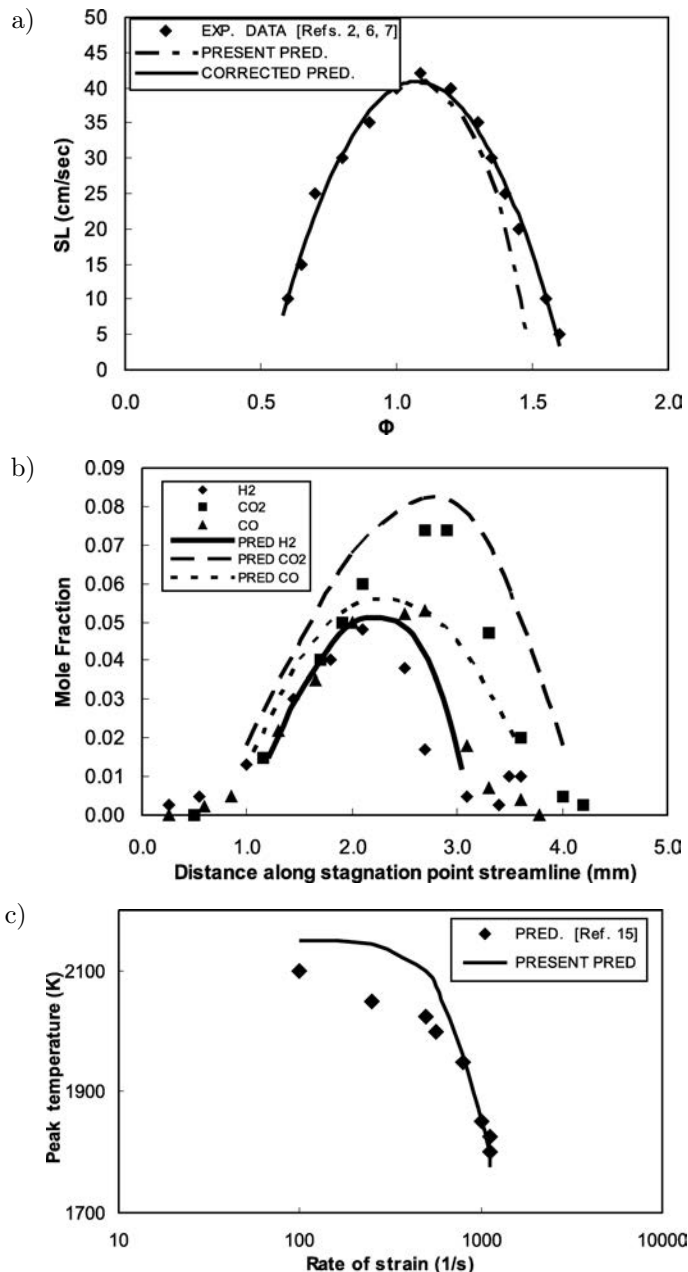
FIG. 1. a) Comparison between computed with the present reduced scheme (- - - -, —) and experimental (♦), Refs. [2, 6], laminar flame speeds over a range of equivalence ratios for freely propagating premixed flames; b) Comparisons between present calculations (lines) and measurements of [14] (points) in a counterflow diffusion flame configuration for major species profiles; c) Peak flame temperature as a function of the strain rate in the stagnation point diffusion flame of Ref. [14]. Computations from Ref. [15] with a four-step reduced mechanism (♦), present computations (—).

elaborate and extended approach along these lines can be applied by following the approach of reference [5] when more involved chemical schemes are adapted to local conditions and constraints.

The reduced scheme (R1) to (R3) was subsequently tested by computing a stagnation point diffusion flame in front of a porous cylinder (Tsuji-type burner, Fig. 3b, [14]) in a one-dimensional calculation by reformulating the detailed mathematical model of Sec. 3. Computed major species and temperature profiles for a strain rate, $a = u_{air,\infty}/R_{cyl}$, of 150 sec^{-1} and a fuel injection velocity v_w of 0.112 m/s (see Fig. 3b), agreed well with the classical experimental results of TSUJI and YAMAOKA [14] as shown in Fig. 1b. The computed unstretched flame peak temperature lies around 1950 K below the adiabatic value due to effects of transport processes and finite reaction rates. The presently calculated drop in the peak temperature with increasing strain rate (a) is adequately supported in similar calculations by JONES and LINDSTEDT [15] as displayed in Fig. 1c. As the strain rate, a, increases the peak temperature drops due to reactant leakage until no steady state solution exists and this point corresponds to the extinction limit. The computed a_{ex} is 645 sec^{-1} while the measurements of reference [14] suggested a value of about 670 sec^{-1}.

Amongst the various flame configurations used for the present scheme calibration, the one selected for discussion here is from the range of opposed jet burner (Fig. 3c) flame studies reported by WEHRMEYER et al. [16]. Specifically the structure of partially premixed opposed jet C_3H_8-air flames produced by counterflowing reactant jets of disparate and very lean or very rich stoichiometry i.e. a lean H_2-air jet impinging on a rich or lean C_3H_8-air jet, was experimentally and computationally investigated in that work (Fig. 3c). The resulting complex type of flames are of relevance to combustion processes occurring under stratified charge mode operation of direct injection spark ignition engines, where a flame in a region of burnable stoichiometry supports combustion in adjacent lean or rich regions that are outside the ignitable limits and thus represent a stringent test of the presented reduced scheme.

Here one partially premixed flame of a C_3H_8-air jet ($\Phi = 1.25$) opposing a H_2-air jet ($\Phi = 0.4$) at a strain rate of 180 s^{-1} was chosen for computation as it represents a stringent test for the proposed model. The results of the comparisons between the present numerical calculations and the measurements and computations, obtained by WEHRMEYER et al. [16], with the extended C_3H_8-air mechanism M5 as reported in Reference [2], are shown in Figs. 2a and 2b. The present computations are in good agreement with the reported temperature and species profiles except for their narrower width due to a slower rise of temperature and species on the rich fuel side. This is due to a weaker penetration of the triple flame into the rich fuel side. This is not unexpected since the uncorrected calibrated reduced sheme produces a lower flame propagation rate, S_L, when

we move toward the rich equivalence ratios, as discussed previously with respect to the underprediction of the experimental S_L branch in Fig. 1a. The calibrated mechanism, when corrected by employing a local adjustment of the (R3) reaction rate preexponential factor as a function of the prevailing local equivalence ratio, results in an improved agreement in the predicted temperature profiles as illustrated in Fig. 2a. The adjusted calculations, due to the locally increased reaction rates, exhibit an extended reaction zone profile that now reaches deeper toward the premixed fuel supply, as indicated by the comparisons shown in Fig. 2a, with consequent improvements in the species profiles as well (lines without correction are not shown for clarity in Fig. 2b).
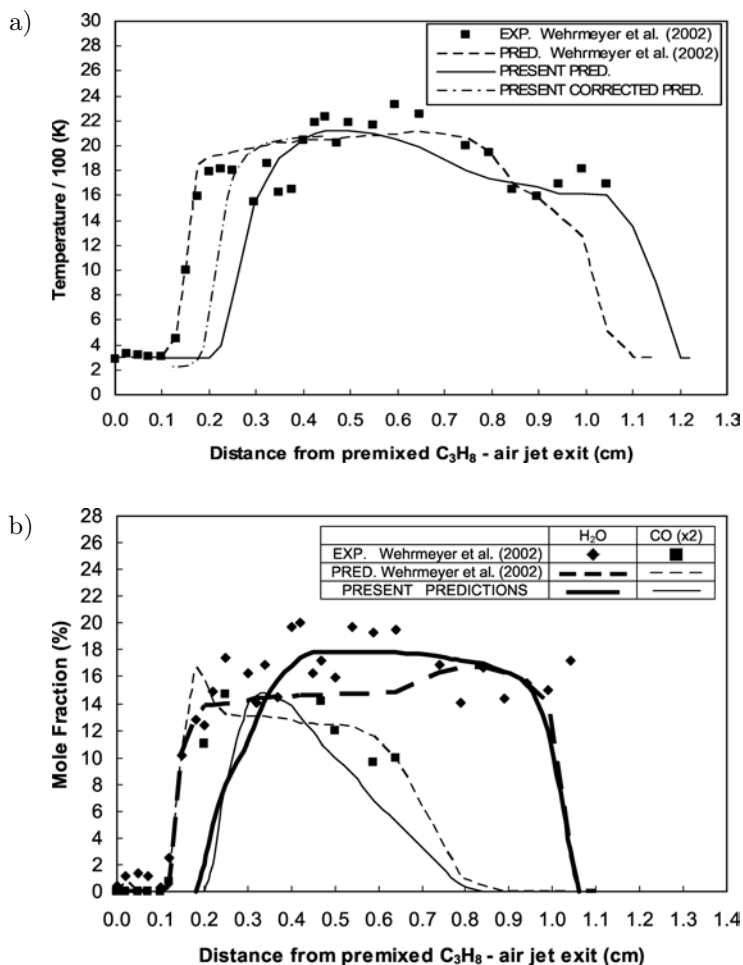
FIG. 2. Comparisons between present calculations (lines) and measurements and computations of WEHRMEYER et al. (symbols, dashed line) in an opposed jet burner premixed flame configuration: a) for the mean temperature profile along the burner stagnation axis; b) for the mean CO and H_2O profiles along the burner stagnation axis.

Subsequently a range of two-dimensional axisymmetric coflowing laminar jet diffusion flames, with or without partial premixing, attached and lifted were calculated targeting at the qualitative and quantitative reproduction of major species, temperature, NO_X and soot production. Any discrepancies identified in these test runs led to readjustment of the reduced chemical scheme rate parameters that were fed back to the runs for the one-dimensional flames discussed above; this iterative cycle produced the final tuned set of the chemical rate parameters of Table 1.

A sketch of the two-dimensional axisymmetric geometry burner configuration employed in the two-dimensional computations is given in Fig. 3a. It includes a fuel supply, an oxidizer supply and in certain test cases – a coflowing surrounding air stream. In the first test case the range of coflowing diffusion flames studied by WON et al. [17] were computed. Fuel (a mixture of C_3H_8/N_2 at 0.1486/0.8514 by mass) and air, both coflowed at various velocity ratios and formed a rich variety of diffusion flames ranging from attached, slightly detached, lifted and also oscillating from the burner rim. Temperature contours predicted by the present two-dimensional formulation employing the above proposed reduced scheme are shown in Figs. 4a, b and c depicting three fuel velocity conditions with none, moderate and significant lift-off from the burner exit. The characteristic fishbone structure at the base as well as the high temperature regions and the overall flame shape have been captured well when compared with the flow visualization photographs reported by WON et al. [17].

[FIG. 3a]

b)

Porous cylinder

Fuel and inert
V_w

flame

Stagnation point

Soot formation
and growth zone

Stagnation streamline

Oxider and inert, u_{∞}

c)

STAGNATION
PLANE

DIFFUSION
FLAME

LEAN
PARTIALLY
PREMIXED
REACTANTS

C_3H_8-Air

RICH
PARTIALLY
PREMIXED
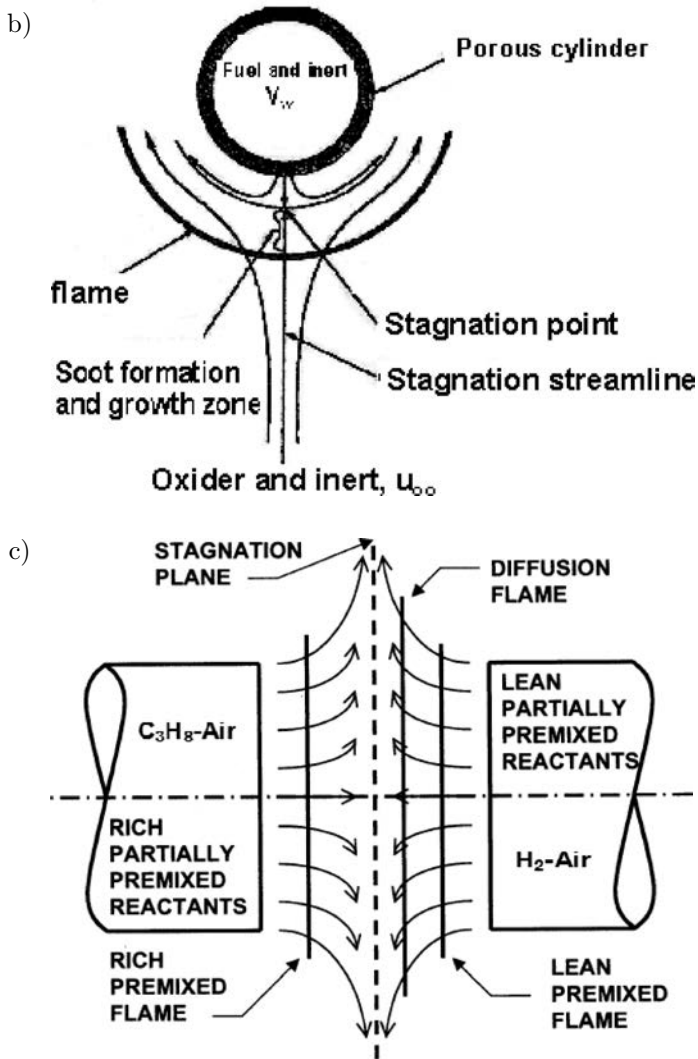REACTANTS

H_2-Air

RICH
PREMIXED
FLAME

LEAN
PREMIXED
FLAME
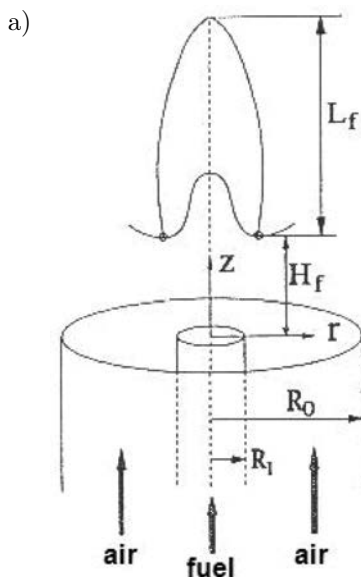
FIG. 3. a) Unconfined coflowing axisymmetric laminar diffusion flame burner configuration used in the computations; b) Porous cylinder counterflow diffusion flame configuration used in the computations (Refs. [14, 20, 21]); c) Opposed jet burner configuration used in the computations (Ref. [16]).

In the experiments of WON *et al.* [17] it was also found that as fuel velocity increases, in the intermediate velocity range, a regime can be identified, where the lift-off height varies intermittently between distinct lower and higher values, a feature that reportedly has been related to propane lift-off behaviour in other investigations as well [17]. As unsteady effects play an important role during localized extinctions and reignitions in highly turbulent flames, it was thought of interest to address the whole extent of the variation of the flame lift-off height
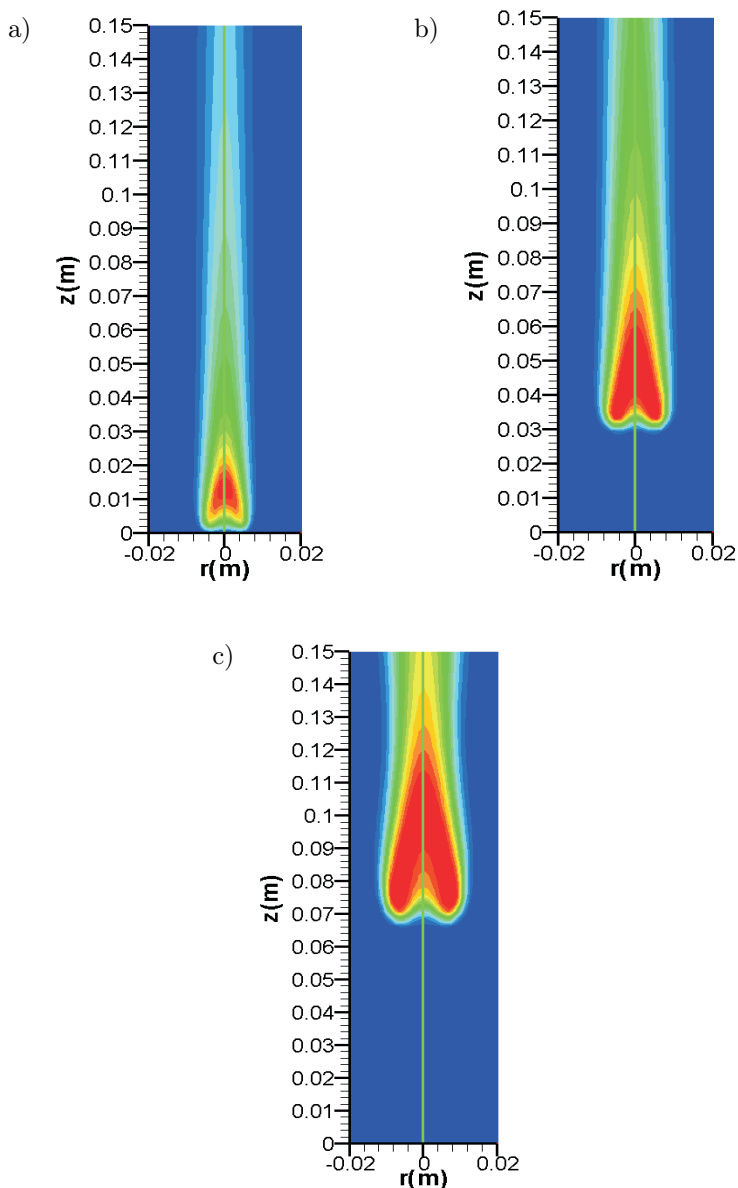
FIG. 4. Computations of temperature isotherm topology for the axisymmetric coflowing jet burner configuration studied by WON *et al.* [17]: a) attached flame, b) moderately lifted flame, c) highly lifted flame.

with fuel velocity change for the flames studied by WON *et al.* [17] to establish the capability of the method to predict inherent unsteady flame behaviour. Figure 5 displays the calculated variation of lift-off height along with the experimentally reported values. Both the attached and lifted flame lengths and lift-off

heights have been reproduced quite satisfactorily while, quite encouragingly, the oscillating flame regime, as indicated by the two branches in the graph, has also been retrieved by the present model. Evidently the presently proposed scheme produces an adequate response to the unsteady strain field produced by the pulsating nature of the flames, despite some quantitative differences in the reported values for the upper lift-off heights.
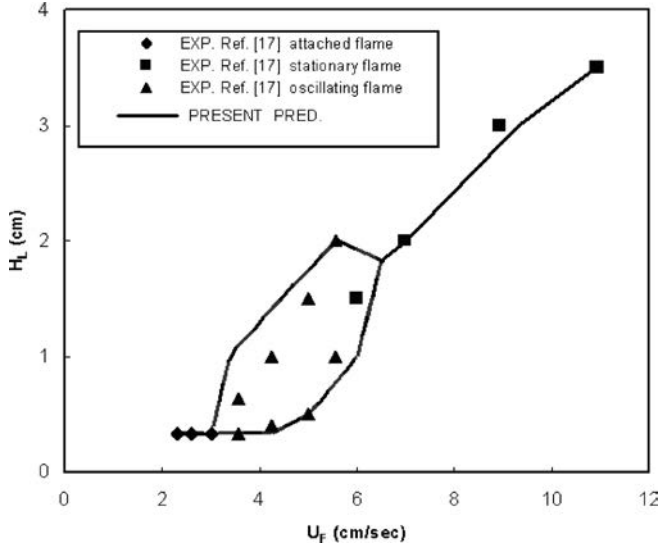
FIG. 5. Comparisons between predicted with the present scheme (line) and experimentally established in WON et al. [17] (symbols) of the variation of the flame lift-off height with fuel exit velocity (note the pulsating flame behaviour indicated by the displayed loop).

Subsequently, the capability of the proposed NOx module to capture the NOx production levels was tested. HEWSON [18] has reported a series of bulk NOx emissions measurements in laminar coflow, nonpremixed jet flames for a wide range of exit propane velocities and burner diameters while retaining the constant air coflow velocity. The reported emission index is expressed as $E_{NOx} = (3X_{NOx}M_{NO2}1000)/(X_{CO2}M_{Fuel})$, where X_i and M_i are the mole fraction and the molecular weight of species i, and this expression includes both the NO and NO_2 contributions. A comparison of the emissions calculated by the presently tuned scheme (the basic oxidation model now including reactions (R4) and (R5)) against a sample from the reported variations is displayed in Fig. 6. Despite the fact that the NO_2 contribution is not accounted for in the present model explicitly but only through tuning and calibration of the constants involved in the prompt rate expressions, the experimental trend and levels are reproduced encouragingly well. As a further test, the NOx levels (including thermal, prompt and N_2O contributions) reported in the work of BOCKHORN et al. [11]
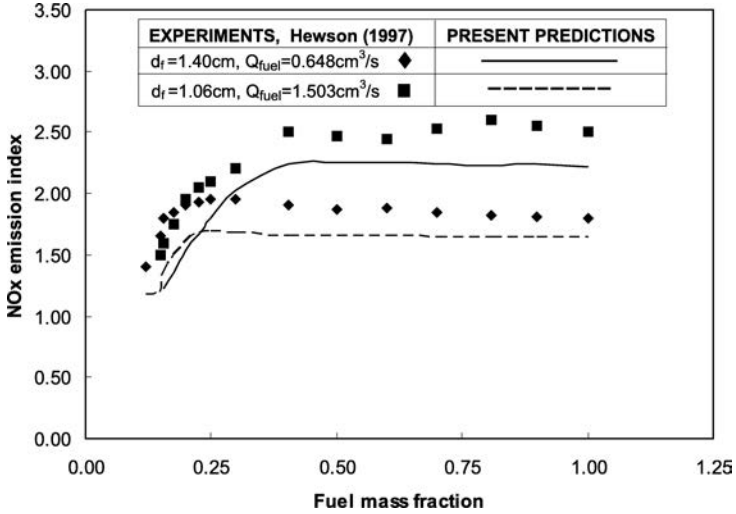
FIG. 6. Comparisons between presently predicted (lines) and experimental (HEWSON [18], symbols) variations of the emission index E_{NOx} with fuel dilution at two fuel velocities in the axisymmetric coflowing burner configuration.

for a range of lean partially premixed 1-D propane flames were additionally studied to further tune the present NOx model. Following the experimental conditions, calculations were run for an inlet mixture temperature of 400°C and a range of equivalence ratios corresponding to an adiabatic flame temperature variation from 1290°C to 1540°C. Results from the present computations are compared, in Fig. 7, with experimental and calculated results reported by
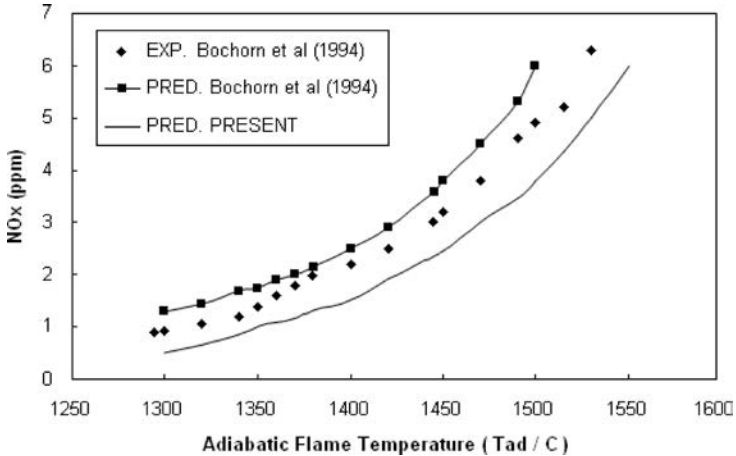
FIG. 7. Comparisons between present predictions (—) and experimental (♦) and computational (—♦—) results from BOCKHORN et al. [11], of the distribution of the NOx concentration levels in a flat premixed 1-D flame burner configuration with variation in the mixture equivalence ratio.

BOCKHORN et al. [11], who employed a version of the GRI 3.0 mechanism (e.g. Ref. [19]). Both the trend and the level of variation of the experimental results with mixture strength are apparently reproduced quite adequately by the tuned ((R4) and (R5) reactions) scheme.

The soot model was finally added to the basic C_3H_8 oxidation mechanism, tuned, calibrated and tested in a range of flame configurations. As an example, calculations for two C_3H_8 sooting counterflow diffusion flame arrangements (Fig. 3b), studied by VANDSBURGER et al. [20] and LAW et al. [21] are here discussed. Additional transport equations with source terms given by Eqs. (3.3) and (3.5) and the reactions (R6) to (R9) were now employed in these computations. The present model predicts the general shape, structure and peak temperature levels of this complex flame configurations. The level of agreement for the major species was of similar good quality as that encountered in the previously discussed computations. Within the context of the present reduced scheme, a critical factor in reproducing the measured soot distributions is the adequate reproduction of the acetylene profile concentrations, the only soot precursor addressed in the reduced scheme, since benzene is here excluded. Levels of C_2H_2 were computed with maximum discrepancies in peak values of less than 12% (e.g. compared with the measured peak values given in reference [20]). The effect of oxygen enrichment in the counterflow flames of VANDSBURGER et al. [20] and the predicted trends in soot production for two levels of fuel enrichment are subsequently shown in Fig. 8. Calculated peak soot volume fractions are in good agreement with experimental values while the variation along the centerline is
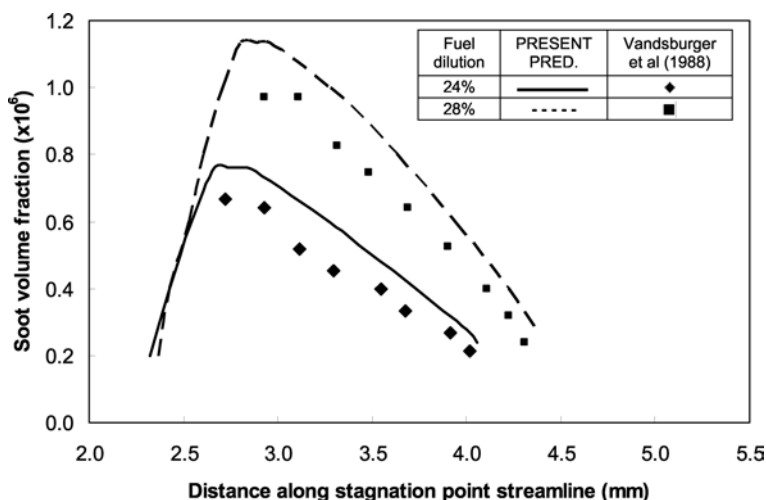
Fuel dilution	PRESENT PRED.	Vandsburger et al (1988)
24%	———	◆
28%	- - - -	■

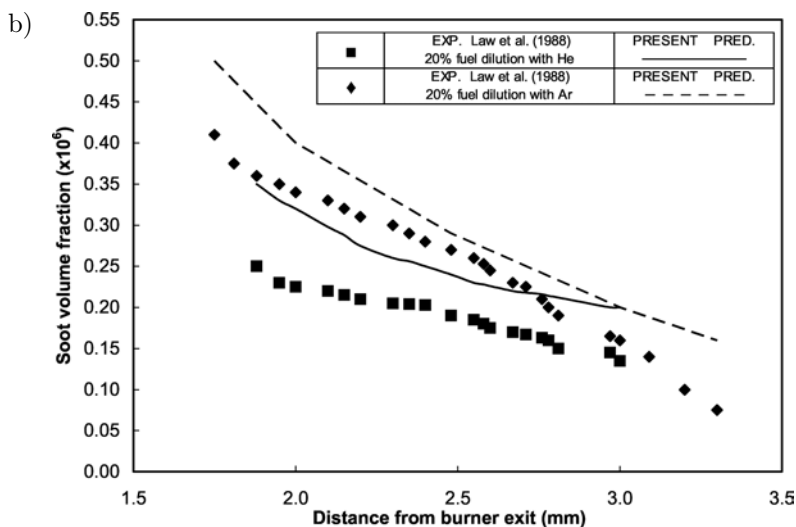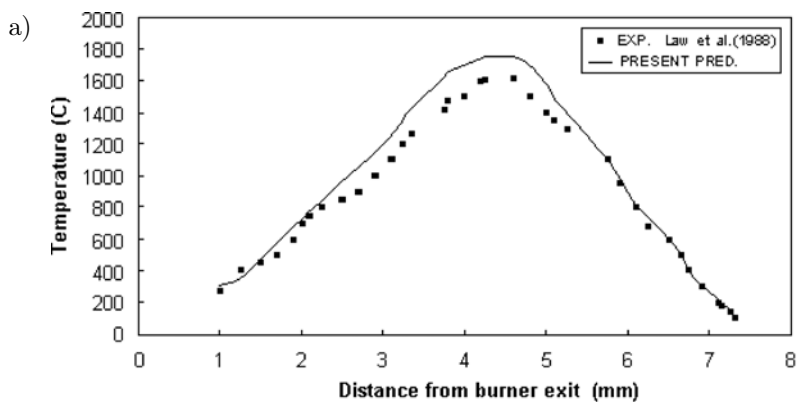FIG. 8. Comparisons between present predictions with the proposed reduced scheme (lines) and experimental and measured by VANDSBURGER et al. [20] (symbols) soot volume fractions for counterflowing C_3H_8-O_2-N_2 flames with varying levels of O_2 enrichment.

captured well. Peak temperatures and major species addressed by the proposed mechanism were also in good agreement with the reported measurements. Next the influence of inert additives and/or air enrichment (25% O_2) in sooting counterflow flames measured by LAW et al. [21] was studied with the above proposed mechanism. Figure 9a displays the measured and presently computed variation of the temperature along the distance from the burner surface for a fuel mixture of 20%He–80%C_3H_8 in this counterflow configuration. The good agreement

FIG. 9. a) Comparisons between present predictions with the proposed reduced scheme (lines) and experimental and measured by LAW et al. [21] temperature distributions with distance from burner exit for propane-air counterflowing diffusion flame with inert addition on the fuel side 2(0%He–80%C_3H_8). b) Comparisons between present predictions with the proposed reduced scheme (lines) and measurements by LAW et al. [21] of soot volume fraction distributions as a function of distance from burner surface for propane-enriched air (25%) counterflowing diffusion flame with different inerts added on the fuel side.

between measurements and predictions allows a meaningful evaluation of the
soot model. Figure 9b displays predictions and experimental data for soot vol-
ume fraction at 20% fuel dilution by two different inert additives, namely He
and Ar and air enrichment with oxygen maintained at 25%. Although some
quantitative discrepancies are evident, it is most encouraging to see that the
measured trends are reproduced quite well. This lends some credibility in the
models sensitivity to delineate between different soot loadings due to different
flame conditions.

From the above described test runs and comparisons it appears that the pro-
posed reduced scheme has an acceptable and consistent behavior over the range
of flame conditions investigated, and adequately predicts the target character-
istics of Sec. 2.1 for the diffusion and premixed flame configurations studied.
Inaccuracies apparently increase locally for rich mixtures beyond an equivalence
ratio of about 1.3 e.g. in the test runs for the lifted flame. This aspect might be
conveniently remedied to a large extent by employing concepts of adaptive chem-
istry as in Reference [5] and locally adjusting (at each computational grid node
and time-step) selected parameters of the reduced scheme in accordance with the
prevailing local flame conditions. Here, following a less involved approach along
these lines proved the promising gains that may accrue from such a more general
procedure; the flame speed was augmented for rich compositions (i.e. when the
mixture strength locally exceeded 1.3) through an appropriate parameterization
and tabulation of the preexponential factor of reaction (R3) as a simple function
of the local equivalence ratio, thus improving the performance of the chemical
scheme over an extented range of mixture compositions.

5. SUMMARY AND CONCLUSIONS

An Integrated Combustion Chemistry approach has been employed to derive
a reduced oxidation scheme for a technically significant fuel, propane, including
submodels for NOx and soot production. The complete scheme involves nine
reactions and nine species focusing on major and stable species and pollutants,
while avoiding altogether the computational burden of intermediate radicals and
elementary rates. The chemical rate parameters were calibrated by systemati-
cally computing a range of well-documented one-dimensional freely propagating,
premixed and stagnation point diffusion flames as well as two-dimensional ax-
isymmetric coflowing jet diffusion flames, lifted and attached. Its overall perfor-
mance has been encouraging and with further tests and refinements it can be
valuable in large-scale computations of complex turbulent reacting flows. The
procedure can be systematically extended to other practical fuels such as higher
hydrocarbons, ethylene or alternative fuels of technological interest such as hy-
drogen, methanol and ethanol.

Acknowledgments

References

1. P. A. Libby and F. A. Williams, *Turbulent reacting flows*, Abacus Press, New York 1993.

2. D. Haworth, B. Cuenot, T. Poinsot and R. Blint, *Numerical simulation of turbulent propane-air combustion with non-homogeneous reactants*, Combustion and Flame, **121**, 395–422, 2000.

3. W. K. Bushe and R. W. Bilger, *Direct numerical simulation of turbulent non-premixed combustion with realistic chemistry*, Annual Research Briefs, Center for Turbulence Research, NASA Ames/Stanford University, 3–22, 1998.

4. P. Koutmos, C. Mavridis and D. Papailiou, *A study of turbulent diffusion flames formed by planar fuel injection into the wake formation region of a slender square cylinder*, Proc. Combust. Inst., **26**, 161–168, 1996.

5. W. H. Green and D. A. Schwer, *Adaptive chemistry*, Computational Fluid and Solid Mechanics, **32**, 1209–1211, 2001.

6. K. M. Leung, P. R. Lindstedt and W. P. Jones, *A simplified reaction mechanism for soot formation in nonpremixed flames*, Combust. and Flame, **87**, 289–305, 1991.

7. C. Kennel, J. Gottgens and N. Peters, *The basic structure of lean C_3H_8 flames*, Proc. Comb. Inst., **23**, 479–485, 1990.

8. U. Mass and S. B. Pope, *Simplifying chemical kinetics: Intrinsic low-dimensional manifolds in composition space*, Combustion and Flame, **88**, 239–264, 1992.

9. B. Bedat, F. N Egolfopoulos and T. Poinsot, *Direct numerical simulations of heat release and NO_X formation in turbulent non-premixed flames*, Combustion and Flame, **119**, 69–83, 1999.

10. P. R. Lindstedt, *Simplified soot nucleation and surface growth steps for non-premixed flames*, [in:] *Soot Formation in Combustion*, H. Bockhorn [Ed.], pp. 417–429, Springer Verlag, Heidelberg 1994.

11. H. Bockhorn, F. Mauss, A. Schlegel, S. Buser, and P. Benz, *NOx formation in lean premixed noncatalytic and catalytically stabilized combustion of propane*, Proc. Combust. Inst., **25**, 1019–1026, 1994.

12. V. R. Katta, L. P. Goss and W. M. Roquemore, *Effect of nonunity Lewis number and finite-rate chemistry on the dynamics of a hydrogen-air jet diffusion flame*, Combustion and Flame, **96**, 60–74, 1994.

13. R. J. Kee, J. F. Grcar, M. D. Smooke and J. A. Miller, *A Fortran program for modeling steady laminar one-dimensional premixed flames*, Sandia National Laboratories, Livenmore, C.A., 1985.

14. H. Tsuji and I. Yamaoka, *Structure analysis of counterflow diffusion flames in the forward stagnation region of a porous cylinder*, Proc. Combust. Inst., **13**, 723–730, 1971.

15. W. P. Jones and P. R. Lindstedt, *The calculation of the structure of laminar counter-flow diffusion flames using a global reaction mechanism*, Combust. and Flame, **61**, 31–49, 1988.

16. J. A. Wehrmeyer, Z. Cheng, D. M. Mosbacher, R. W. Pitz, and R. Osborne, *Opposed jet flames of lean or rich premixed propane-air reactants versus hot products*, Combust. and Flame, **128**, 232–241, 2002.

17. S. H. Won, S. H. Chung, M. S. Cha, and B. J. Lee, *Lifted flame stabilization in developing and developed regions of coflow jets for highly diluted propane*, Proc. Combust. Inst., **28**, 2093–2099, 2000.

18. J. C. Hewson, *Pollutant emissions from nonpremixed hydrocarbon flames*, PhD. Thesis, University of California, San Diego 1997.

19. G. P. Smith, D. M. Golden, M. Frenklach, N. W. Moriarty, B. Eitener *et al.*, GRI-Mech version 3.0, http://www.me.berkeley.edu/gri-mech/

20. U. Vandsburger, I. Kennedy, and I. Glassman, *Soot formation in oxygen enriched counterflow diffusion flames of C_2H_4 and C_3H_8*, Combust. Sci. and Technol., **39**, 263–285, 1984.

21. C. K. Law, R. L. Axelbaum, and W. L. Flower, *Preferential diffusion and concentration modification in sooting counterflow diffusion flames*, Proc. Combust. Inst., **22**, 379–386, 1988.

DYNAMICS OF THE COMPLEX SYSTEM WITH ELASTIC AND VISCO-ELASTIC INERTIAL INTERLAYERS

K. C a b a ń s k a – P ł a c z k i e w i c z

The Kazimierz Wielki University in Bydgoszcz
Faculty of Mathematics, Physics and Technology
Institute of Technology

30 Chodkiewicza street, 85-064 Bydgoszcz, Poland

In this paper is given the dynamic analysis of the free and forced vibration problems of a complex system with elastic and visco-elastic inertial interlayers. The analytical method of solving the free and forced vibrations problem of the system is presented in the paper [2]. The external layer of the complex system is treated as the plate made from elastic materials, coupled by visco-elastic inertial interlayers. The plate is described by the Kirchhoff–Love model. The visco-elastic, inertial interlayer possesses the characteristics of a continuous inertial Winkler foundation and has been described by the Voigt-Kelvin model. Small transverse displacements of the complex system are excited by the stationary and non-stationary dynamical loadings. The phenomenon of free and forced vibrations problems has been described using a non-homogeneous system of conjugate, partial differential equations. After separation of variables in the homogeneous system, the boundary value problem has been solved and two sequences have been obtained: the sequences of frequencies and the sequences of free vibrations modes. Then, the property of orthogonality of complex free vibrations has been presented. The free vibrations problem has been solved for some arbitrarily assumed initial conditions. The forced vibrations problem has been considered for different modes of dynamical loading [3].

The solution of the ecological safety problem and protection from exposure to dust, depend much on the equipment and techniques used in quarrying the brown coal. Thus, dynamics of loading the open cast colliery dump trucks which have a load-carrying capacity of hundreds of tons, mass of tens of tons and dimensions of tens of meters, is a very important problem. The numerical results of free and forced vibrations problems of the complex system with the elastic and visco-elastic inertial interlayer, for various parameters and different modes of dynamical loading, are given in this paper.

Key words: vibrations, two-layer system, damping, numerical results.

1. Introduction

The problems of vibrations with damping of complex structures play an important role in various engineering structures. Some mechanical and building constructional systems consisting of strings, beams, shafts, plates and shells, can

be connected by elastic or visco-elastic constraints, working in complex conditions of stationary and non-stationary loading. In dynamics of various technical objects important influence on their character operation is exerted by unavoidable vibrations of certain structural elements.

A typical example of the above-mentioned constructional elements can be layers, which are made of soft elastic or visco-elastic materials. On this subject, the mathematical method was presented by CABAŃSKA–PŁACZKIEWICZ [3] taking into account not only stationary loading of complex systems using the methods based on the Kirchhoff–Love hypothesis [8], but also non-stationary loading of complex systems based on the TIMOSHENKO model [26]. Among numerous precise models applied to the investigation of plates made of modern materials, the REISNER model [21] was used.

Wide bibliography concerning the classical, rheological models, were presented by NASHIF, JONES, HENDERSON [12], NOWACKI [14], RYMARZ [23] and the operator methods were given by OSIOWSKI [18].

In the paper by JEMIELITA [7], the criteria of choice of the shear coefficient in plates of medium thickness have been considered. Vibrations of elastic compound systems subjected to inertial moving load was presented by BOGACZ [1], ONISZCZUK [15, 16] using the Renaudot formula [22] and SZCZEŚNIAK [24, 25].

The problem of non-axisymmetric deformation of flexible rotational shells was solved by PANKRATOVA, NIKOLAEV, ŚWITOŃSKI [19] using the classical Kirchhoff-Love model and the improved TIMOSHENKO model. The dynamic problem of elastic homogeneous bodies was presented by TARANTO, MC GRAW [6], KURNIK, TYLIKOWSKI [10, 28], MINDLIN, SCHACKNOW [1], PANKRATOVA, MUKOED [20] and WANG [29]. The interlayer is a one- or two-directional viscoelastic WINKLER [30] layer, but it can also be a multiparametric viscoelastic layer presented by WOŹNIAK [31].

In the above-mentioned complex cases, especially where viscosity and discrete elements occur, it is recommended to adopt the method of solving the dynamic problem of a system in the domain of functions of complex variable, following the papers by TSE, MORSE, HINKLE [27], NIZIOŁ, SNAMINA [13] and CABAŃSKA–PŁACZKIEWICZ [2–3]. The property of orthogonality of free vibrations of complex types was first described by CREMER, HECKEL, UNGAR [5] and CABAŃSKI [4] or discrete systems with damping, and for discrete – continuous systems with damping – by NASHIF, JOHNES and HENDERSON [12], and for continuous systems with damping – by NOWACKI [14].

The aim of this paper is a dynamics analysis of a complex system with elastic and visco-elastic interlayers for various geometrical, physical and mechanical parameters, and for different modes of dynamical loading.

2. Problems of control of vibrations in ecologically-dangerous technical systems

2.1. Statement of the problem

Interdisciplinary range of problems connected with development and use of brown coal, is extremely urgent for Central and Western Europe. The practical significance of these problems is determined by many factors. One of them that should be noticed is that 58% of world productions of brown coal is concentrated in the given region. Life of lignite reserves is in excess of 240 years. Poland is one of the world leaders in this field and takes the 4-th place after Germany, Russia and USA. Therefore, great attention of engineering universities in Poland is given to various research aspects and directions within the given range of problems. A problem of ecological safety and protection of mine staff and inhabitants of the surrounding areas from exposure to dust, takes an important place among them.

For example, the capacity of the body of a dump truck is 337 m^3, its width is 8.53 m, length is 15.54 m, depth is 3.34 m and mass is tons. The analysis shows that the volume of dust ejection during loading of coal depends on the efficiency of control of body vibrations by the shock-absorbing system of a dump truck. At the same time, the standard models and methods of analysis and control of mechanical vibrations, are based on a combination of the control and vibration theories.

Thus, the analysis of dynamic response and of non-linear body vibrations is usually made with the help of models where the body is schematically represented as a load resting on a spring with one or several degrees of freedom. Such an approach does not take into account certain essential properties of dynamics of loading. These are, for instance, irregularity of loading the body, randomness of distribution of a shock dynamic loading over the surface of a body, dynamics of interaction of a body and a dump truck during the shock load. Therefore, there is a practical necessity for making a common formulation of the problem of analysing and controlling the vibrations of open cast colliery dump trucks as an interdisciplinary problem of vibration theory, control theory and visco-elastic theory. The last one takes into account real processes of a dynamic response during the action of a non-uniform shock loading on a real structure of a dump truck body on the whole.

It should be remembered that the dynamics of operation of material system is always influenced by the residual vibrations.

Typical examples concern the important dynamic problems of certain objects working in the open extraction of coal in Poland, e. g. deep-immersion at subsoil motors, truck and the special spring balances on which are resting many tons of

coal mass. The dynamical problems occur also in the railroad engineering and the seaports, e.g. in the shock occurring by cargoes of a cargo ship.

In the design of such objects, an important practical meaning has the optimal choice of the main factors of the vibrational processes, providing the optimal compromise of controversial requirements to the dynamic elements system: shock-absorber-weight.

Let us consider stationary and non-stationary dynamical loading of complex system with damping (Fig. 1). The complex system is made from the elastic plate which is coupled by a visco-elastic inertial interlayer resting on a stiff foundation. The elastic plate is described as the Kirchhoff–Love model [8], and is simply supported at their edges. The interlayer connecting the plate with the rigid foundation [30, 31] will be replaced in further considerations by the so-called simplified foundation, which is modelled as the homogeneous foundation. Besides it is assumed that this simplified foundation consist of a close-packed set of homogeneous pillars appearing within the plate contour.
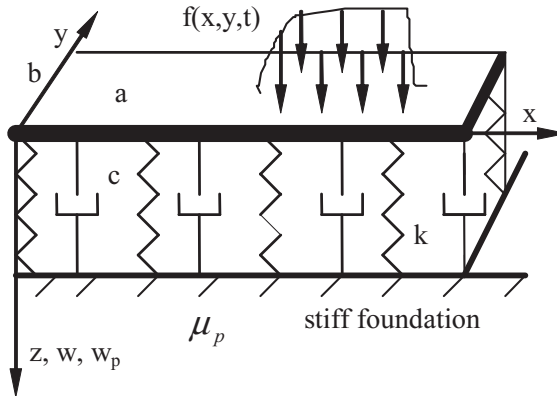
FIG. 1. Dynamic model of an elastic plate coupled with a visco-elastic inertial interlayer, under the stationary and non-stationary dynamical loading.

For this reason, the strains in the directions of co-ordinate axes x and y are equal to zero. Each of the pillars with unit area of cross-section, has length equal to thickness of this foundation and is made of visco-elastic material described by the Voigt–Kelvin model [12, 14, 17].

Due to the small angle of slope of the deflection surface of the plate, the shearing forces acting on lateral faces of these pillars are also very small and hence they can be neglected.

On grounds of the above assumed simplification it follows that these pillars are subjected to uniaxial strain but to the three-dimensional state of stress.

It is obvious that the displacement of the simplified foundation is identified with the displacement of the corresponding pillar which is placed at the point of

co-ordinates x, y. In this situation these displacements are apparently described by a one-dimensional differential equation; nevertheless it should be observed that these displacements are not only dependent on the variable z, but also on the variables x, y.

In practical application, the combined system (Fig. 1) is treated as a platform with the stationary and non-stationary dynamical, concentrated or distributed loadings by the moving mass of coal [2, 3].

2.2. Mathematical problem

The phenomenon of small transverse vibrations of the elastic plate coupled with a visco-elastic inertial interlayer is described by the following non-homogeneous system of conjugate partial differential equations [2]:

$$D\Delta^2 w + \mu\frac{\partial^2 w}{\partial t^2} - \left(1 + c\frac{\partial}{\partial t}\right)k\frac{\partial w_p}{\partial z}\Big|_{z=0} = f(x,y,t),$$

(2.1)

$$\left(1 + c\frac{\partial}{\partial t}\right)k\frac{\partial^2 w_p}{\partial z^2} - \mu_p\frac{\partial^2 w_p}{\partial t^2} = 0$$

together with the corresponding homogeneous boundary conditions for the plate

(2.2a)
$$w\big|_{x=0} = 0, \qquad w\big|_{x=a} = 0, \qquad w\big|_{y=0} = 0, \qquad w\big|_{y=b} = 0,$$

$$\frac{\partial^2 w}{\partial x^2}\Big|_{x=0} = 0, \qquad \frac{\partial^2 w}{\partial x^2}\Big|_{x=a} = 0, \qquad \frac{\partial^2 w}{\partial y^2}\Big|_{y=0} = 0, \qquad \frac{\partial^2 w}{\partial y^2}\Big|_{y=b} = 0$$

and for the inertial foundation

(2.2b)
$$w_p\big|_{z=h_p} = 0,$$

as well as with the continuity condition of displacements of the plate and the simplified foundation

(2.2c)
$$w = w_p\big|_{z=0}.$$

In Eq. (2.1) are introduced the following notations:

(2.3) $$D = \frac{Eh^3}{12(1-\nu_o^2)}, \qquad k = \frac{E_p(1-\nu_p)}{(1-2\nu_p)(1+\nu_p)}, \qquad \mu = \rho h, \qquad \mu_p = \rho_p.$$

Here $f(x,y,t)$ is the dynamical load of the complex system; $w = w(x,y,t)$, $w_p = w_p(x,y,z,t)$ are the transverse deflections of the plate and the visco-elastic

inertial interlayer; E, E_p are the Young modulus of materials of the plate and the interlayer; c is the damping coefficient of the interlayer (retardation time); ρ, ρ_p are the mass densities of materials of the plate and the interlayer; h, h_p are the thicknesses of the plate and the interlayer; a, b are the dimensions of the complex system; ν_o, ν_p is the Poisson coefficient of the plate and the interlayer; x, y are the co-ordinate axes.

An analytical method of solving the problem of boundary-value problem as well as free and forced vibrations of mechanical system (Fig. 1), will be based on separation of variables.

Substituting the following dependences:

(2.4) $$w = WT, \qquad w_p = W_p T$$

into the system of differential equations (2.1), one obtains the ordinary differential equation

(2.5) $$\overset{o}{T} - i\nu T = 0$$

and the system of partial differential equations

(2.6) $$D\Delta^2 W - \nu^2 \mu W - (1 + i\nu c)k \left.\frac{dW_p}{dz}\right|_{z=0} = 0,$$

$$(1 + ic\nu)R + \nu^2 \mu_p W_p = 0,$$

where $T = T(t)$ denotes the modal function; $W = W(x, y)$ and $W_p = W_p(x, y, z)$ stand for complex modes of vibration of the plate and the layer; ν is the complex eigenfrequency of vibrations.

Thanks to the relations (2.4), the boundary conditions (2.2) take the following form:

$$W\,|_{x=0} = 0, \qquad W\,|_{x=a} = 0, \qquad W\,|_{y=0} = 0, \qquad W\,|_{y=b} = 0,$$

(2.7) $$\left.\frac{\partial^2 W}{\partial x^2}\right|_{x=0} = 0, \quad \left.\frac{\partial^2 W}{\partial x^2}\right|_{x=a} = 0, \quad \left.\frac{\partial^2 W}{\partial y^2}\right|_{y=0} = 0, \quad \left.\frac{\partial^2 W}{\partial y^2}\right|_{y=b} = 0,$$

$$W_p\,|_{z=h_p} = 0, \quad W = W_p\,|_{z=0}\,.$$

Further analytical procedures of solving this problem are presented in the papers [1, 2, 3, 24, 25].

2.3. Different modes of dynamical loading

In the first case, small transverse vibrations of the complex system with damping are excited by the following stationary, concentrated dynamical loading

(2.8) $f(x, y, t) = P\delta(x - x_o)\delta(y - y_o)\sin(\omega_o t)$

at the point x_o, y_o and varying in time t.

In the second case, small transverse vibrations of the complex system with damping are excited by the following non-stationary concentrated dynamical loading

(2.9) $f(x, y, t) = b(t) - m\dfrac{d^2\overline{w}(x^*, y_o, t)}{dt^2}\delta(x - x^*)\delta(y - y_o),$

or by the following non-stationary concentrated dynamical loading:

(2.10) $f(x, y, t) = b(t) - \dfrac{m}{d}\dfrac{d^2\overline{w}(x^*, y_o, t)}{dt^2}[H(x - x^* - d) - H(x - x^*)].$

Here m is the mass of coal; d is the length on which the moving mass is distributed; $\delta(...)$ is the Dirac delta function; $H(...)$ is the Heaviside function; $x^* = v^* t$, v^* is the constant speed; $y_o = 0.5b$; $\overline{w}(x^*, y_o, t)$ denote the transverse displacements of the plate in its first approximation at the points of location of the moving mass of coal, i.e. the trajectory of the moving mass of coal; P is the amplitude of harmonic force; $f(x, y, t)$ is the dynamical loading of the complex plate; v_n are complex frequencies of free vibrations; x_o, y_o are the co-ordinate coal for time $t = 0$; $b(t)$ is the constant loading in the direction of axis z.

3. Results and discussions

Calculations are carried out for the following data:
$E = 10^{10}$ Pa, $E_p = \gamma^* 10^8$ Pa, $\nu_o = 0.3$, $\nu_p = 0.2$, $\rho = 5^* 10^3$ Ns^2 m^{-4}, $\rho_p = 7^* 10^3$ Ns^2 m^{-4}, $h = 0.5$ m, $h_p = \varepsilon^* 3.34$ m, $a = 15.54$ m, $b = 8.53$ m, $c = \wp^* 0.00007$ Nsm^{-2}, $b(t) = 0$, $v^* = \varsigma^* 10$ ms^{-1}, $c_g = 0.00001$, $\omega_n = \mathrm{Re}[\nu_n]$, $P = 4^* 10^2$ kN, $m = 4^* 10^4$ kg.

In order to solve the boundary value problem, the following boundary conditions are used for the Kirchhoff–Love model.

Let us consider the free and forced vibrations problem of the complex system (see Fig. 1).

In order to find the Fourier coefficient $\varPhi_{n_1 n_2}$, the following initial conditions are assumed:

(3.1) $w_o = A_{s1}\sin\left(\dfrac{\pi x}{a}\right)\sin\left(\dfrac{\pi y}{b}\right),$ $\overset{o}{w}_o = 0,$ $A_s = 0.0016\, m$

where w_o is the initial displacement; $\overset{o}{w}_o$ is the initial velocity.

Some results of this problem given in Fig. 2 present absolute values of a complex determinant $|\Delta|$ and eigenfrequencies of free vibrations. The diagrams

of the values of complex eigenfrequencies $\nu_{n_1 n_2} = i\eta_{n_1 n_2} \pm \omega_{n_1 n_2}$ of free vibrations for various parameters $\wp = 1$, $g = 1$, $\gamma = 1; 0.01; 0.0001$, $\varepsilon = 1; 0.6; 0.3$ are shown in Fig. 2.
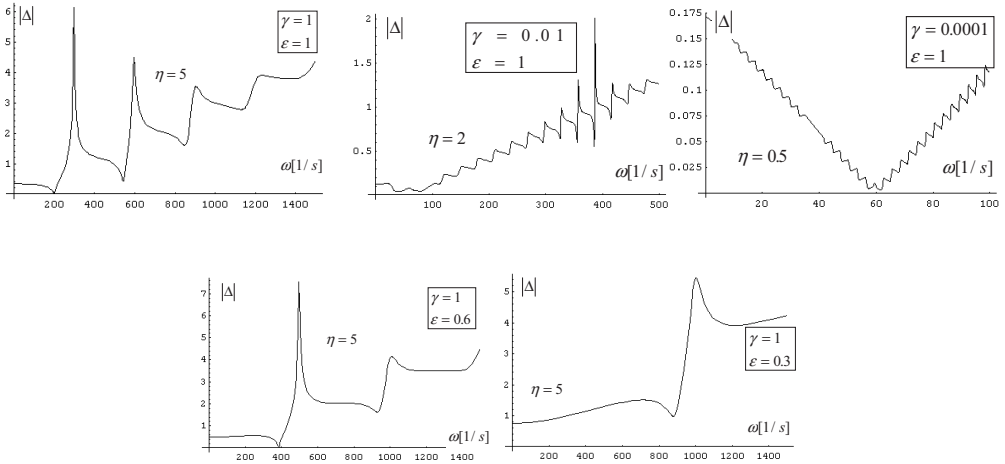

FIG. 2. Moduli of a complex determinant $|\Delta|$ and values of complex eigenfrequencies $\nu_{n_1 n_2} = i\eta_{n_1 n_2} \pm \omega_{n_1 n_2}$ of free vibrations for $x = 0.6a$, $y = 0.6b$, $z = 0$ and $n_1 = 1$, $n_2 = 1$.

The space diagrams in Fig. 3 shows complex modes of free vibration of the visco-elastic inertial interlayer for $n_1 = 1$, $n_2 = 1$ and $n_1 = 1$, $n_2 = 2$. The space diagrams of $W(x)$ show the real ReW and the imaginary ImW parts of complex modes of free vibrations of the interlayer, in the ranges $0 < x < a$ and $0 < z < h$ and $y = 0.5b$. For $z = 0$, the diagrams show the real ReW_1 and the imaginary ImW_1 parts of complex modes of free vibrations of the plate.

The diagrams in Fig. 4 show free vibrations of the complex system with elastic and visco-elastic interlayers in time t in two cases; the first case where damping coefficient $\wp = 1$ occurs, the second case where damping coefficient does not occur, $\wp = 0$.

Calculations of dynamic displacements for the two cases where damping coefficient occurs $\wp = 1$, are compared with dynamic displacements in which the damping coefficient does not occur, $\wp = 0$ – Fig. 4. Amplitudes of free vibrations for damping coefficient $\wp = 1$ in a visco-elastic interlayer have the value approximately by 62% smaller than the amplitudes of free vibrations for the damping coefficient $\wp = 0$ in the elastic interlayer of the complex system.

The effects of various geometrical physical and mechanical parameters are shown in Figs. 5–12. In the first case, small transverse vibrations of the complex system with a viscoelastic inertial interlayer are excited by the stationary dynamical force (2.7) acting at the point $x = 0.6a$, $y - 0.6b$, $z = 0$ and varying in time t.
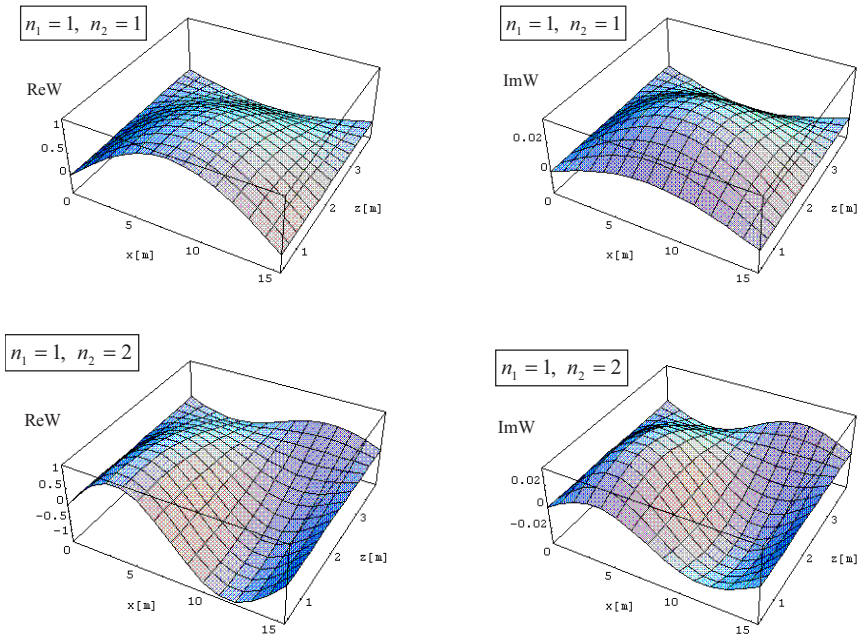
FIG. 3. Complex modes of free vibrations of the complex system with damping for $n_1 = 1$, $n_2 = 1$ and $n_1 = 1$, $n_2 = 2$; the elastic plate for $z = 0$ and the visco-elastic inertial interlayer for $0 < z < h$.
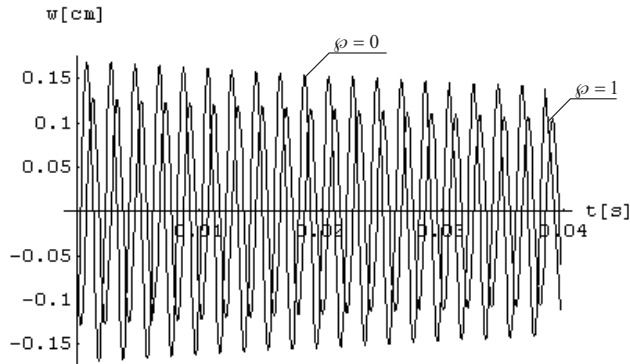

FIG. 4. Free vibrations of the complex system with the elastic $\wp = 0$ and visco-elastic $\wp = 1$ inertial interlayers for $\gamma = 1$, $\varepsilon = 1$.

The effect of stationary dynamical force in the complex system with elastic and visco-elastic interlayer is presented in Figs. 5–9 for various damping coefficients of the interlayer: $\wp = 0$ (Figs. 5a–9a) and $\wp = 1$ (Figs. 5b–9b).

In the case when the complex system is loaded by stationary concentrated force and for damping coefficient of the visco-elastic interlayer $\wp = 1$ (Figs. 5b–9b),

the amplitudes of forced vibrations achieve a value approximately 55–63% smaller than the amplitudes of forced vibrations for damping coefficient of the elastic interlayer $\wp = 0$ (Figs. 5a–9a).

The effects of stationary dynamical force in the complex system with visco-elastic inertial interlayer $\wp = 1$ are presented in Fig. 5b for the theoretical A and experimental A^* investigations.

In the case when the complex system is loaded by a stationary dynamical force, for the experimental amplitudes A^* of forced vibrations we obtain a value approximately 7% smaller than the amplitudes of forced vibrations for the analytical amplitudes A.

a)   b)
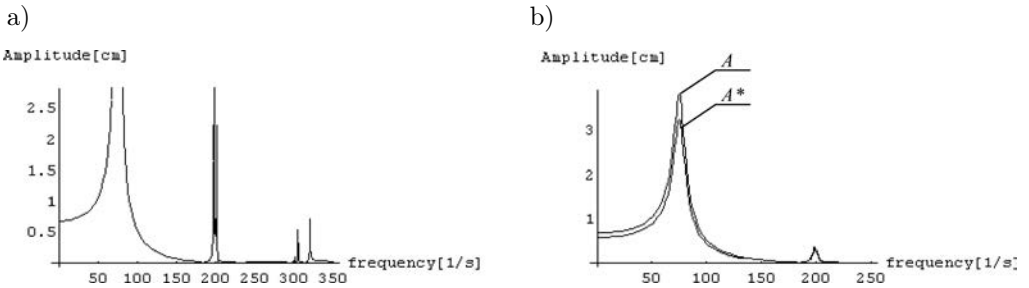
FIG. 5. Forced vibrations of the complex system for the stationary force and $\gamma = 1$, $\varepsilon = 1$; a) $\wp = 0$, b) $\wp = 1$.
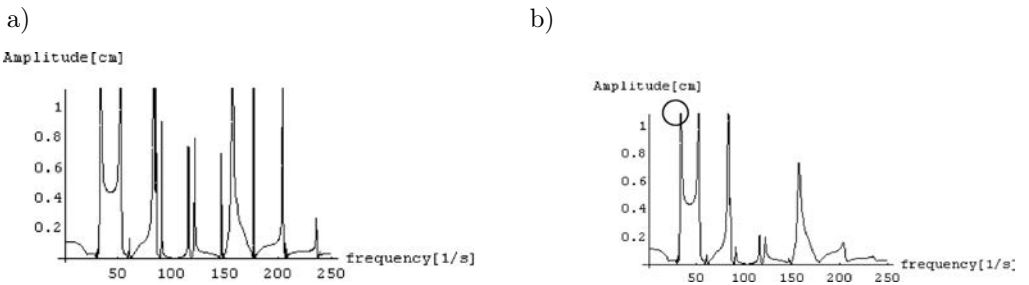
a)   b)

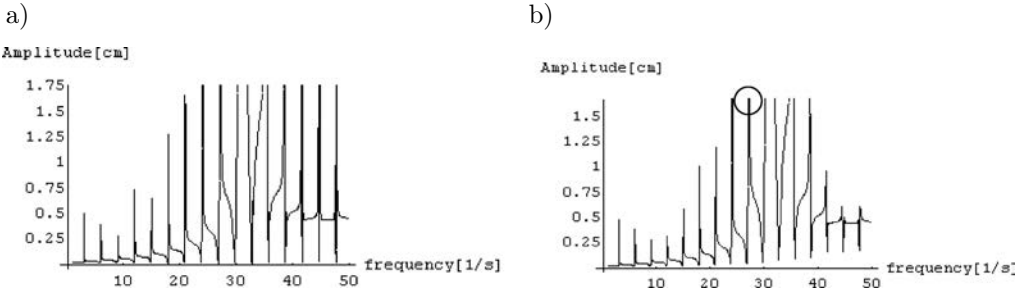FIG. 6. Forced vibrations of the complex system for the stationary force and $\gamma = 0.01$, $\varepsilon = 1$; a) $\wp = 0$, b) $\wp = 1$.

After analysing the results presented in Figs. 5b–9b where damping coefficient in the interlayer occurs, we state that the visco-elastic inertial interlayer can be a vibration damper for the elastic plate which is loaded by the stationary dynamical force acting at the point $x = 0.6a$, $y = 0.6b$ and varying in time t.

In the case when the damping coefficient is equal to zero, presented in Figs. 5a–9a, resonance in the complex plate with an elastic inertial interlayer occurs, because real frequency $\pm\omega_{n_1 n_2}$ of free vibrations is coinciding with real frequency ω_o of forced vibrations. In the case when damping coefficient is dif-

ferent from zero, presented in Figs. 5b–9b, no resonance in the complex plate with a visco-elastic inertial interlayer, because complex eigenfrequency $\nu_{n_1 n_2} = i\eta_{n_1 n_2} \pm \omega_{n_1 n_2}$ of free vibrations (Fig. 2) is do not coinciding with real frequency ω_o of forced vibrations.

The effect of stationary dynamical force in the complex system with a visco-elastic interlayer is presented in Figs. 5–7 for the various Young moduli of the interlayer $\gamma = 1$ (Fig. 5), $\gamma = 0.01$ (Fig. 6) and $\gamma = 0.0001$ (Fig. 7).

a)   b)

FIG. 7. Forced vibrations of the complex system for the stationary force and $\gamma = 0.0001$, $\varepsilon = 1$; a) $\wp = 0$, b) $\wp = 1$.

In the case when the complex system with damping is loaded by the stationary dynamical force, for the Young modulus of the visco-elastic interlayer $\gamma = 1$ (Fig. 5), the amplitudes of forced vibrations achieve a value approximately 65% smaller than the amplitudes of forced vibrations for the Young modulus of the visco-elastic interlayer $\gamma = 0.01$ (Fig. 6). For the Young modulus of the visco-elastic interlayer $\gamma = 0.01$ (Fig. 6), the amplitudes of forced vibrations achieve a value approximately 60% smaller than the amplitudes of forced vibrations for the Young modulus of the visco-elastic interlayer $\gamma = 0.0001$ (Fig. 7).

The effect of stationary dynamical force in the complex system with a visco-elastic interlayer is presented in Figs. 5, 8, 9 for various thicknesses of the interlayer $\varepsilon = 1$ (Fig. 5), $\varepsilon = 0.6$ (Fig. 8) and $\varepsilon = 0.3$ (Fig. 9).
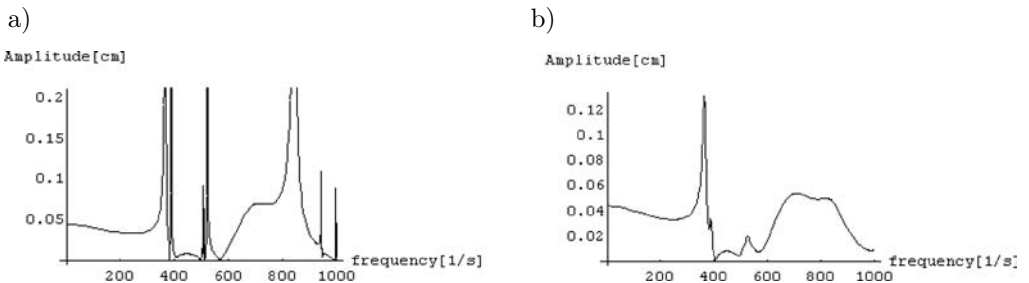
a)   b)

FIG. 8. Forced vibrations of the complex system for the stationary force and $\gamma = 1$, $\varepsilon = 0.6$; a) $\wp = 0$, b) $\wp = 1$.
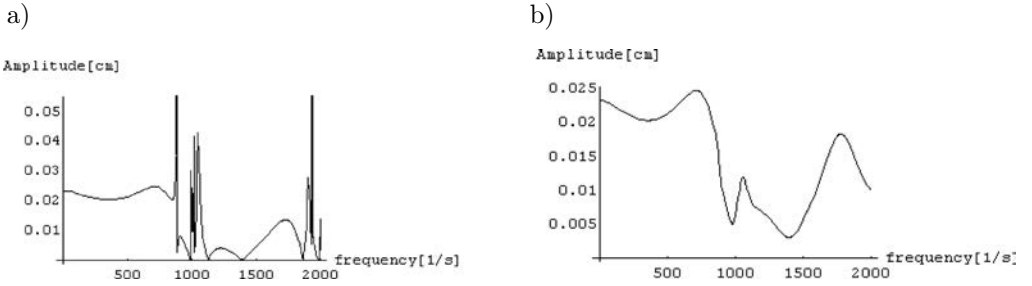
a)   b)

FIG. 9. Forced vibrations of the complex system for the stationary force and $\gamma = 0$, $\varepsilon = 0.3$;
a) $\wp = 0$, b) $\wp = 1$.

In the case when the complex system with damping is loaded by the station-
ary dynamical force, for a small thickness of the visco-elastic interlayer $\varepsilon = 0.3$
(Fig. 9) the amplitudes of forced vibrations achieve a value approximately 79%
smaller than amplitudes of forced vibrations for a large thickness of the visco-
elastic interlayer $\varepsilon = 0.6$ (Fig. 8). For a small thickness of the visco-elastic
interlayer $\varepsilon = 0.6$ (Fig. 8), the amplitudes of forced vibrations achieve a value
approximately 95% smaller than the amplitudes of forced vibrations for a large
thickness of the visco-elastic interlayer $\varepsilon = 1$ (Fig. 5).

In the second case, small transverse vibrations of the complex system with
a visco-elastic inertial interlayer are excited by the dynamical non-stationary
loading expressed by the equations (2.8) or (2.9). The mass is moving with the
speed ς for $y = 0.5b$.

The effect of moving mass in the complex system with a visco-elastic inertial
interlayer is presented in Fig. 10 for various speeds $\varsigma = \{1, 2, 3, 5, 6\}$ and various
damping coefficients $\wp = \{0, 0.6, 1\}$.

In the case when the complex system is loaded by a moving mass and when
the damping coefficient of the visco-elastic interlayer $\wp = 1$, the amplitudes of
forced vibrations achieve a value approximately 20–30% smaller than the ampli-
tudes of forced vibrations for damping coefficient of the visco-elastic interlayer
$\wp = 0.6$. In the case when the complex system is loaded by a moving mass
and when the damping coefficient of the visco-elastic interlayer $\wp = 0.6$, the
amplitudes of forced vibrations achieve a value approximately 50–60% smaller
than the amplitudes of forced vibrations for damping coefficient of the elastic
interlayer $\wp = 0$ (Fig. 10).

In the case when the complex system with damping is loaded by the mass
moving with speed $\varsigma = 1$, the amplitudes of forced vibrations achieve a value
approximately 10% smaller than the amplitudes of forced vibrations for the
speed $\varsigma = 2$. In the case when the complex system with damping is loaded
by the moving mass with the speed $\varsigma = 2$, the amplitudes of forced vibrations
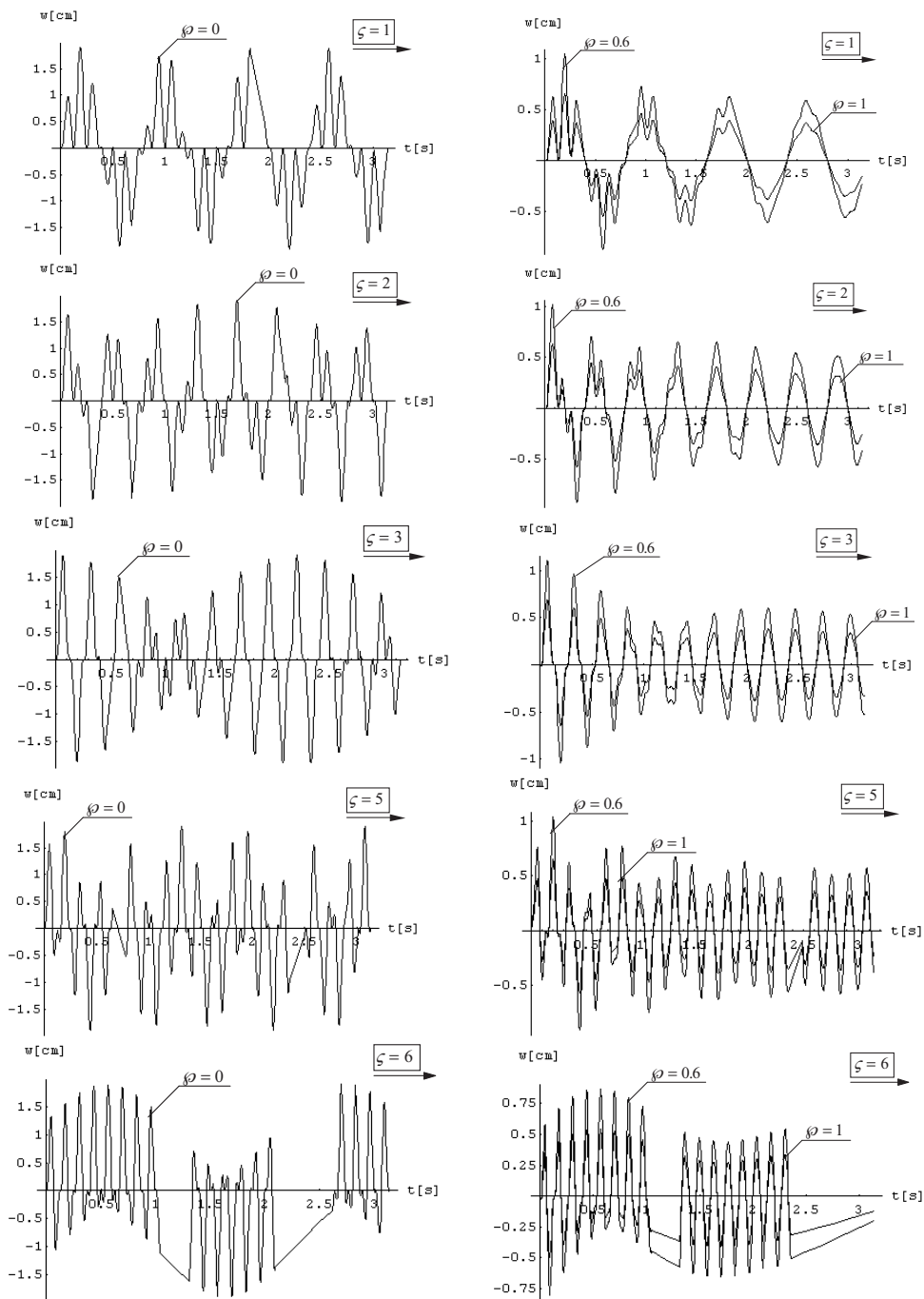
FIG. 10. Forced vibrations of the elastic and visco-elastic complex system for the moving mass with the speeds $\varsigma = \{1, 2, 3, 5, 6\}$ for $\gamma = 1$, $\varepsilon = 1$, $\wp = \{0, 0.6, 1\}$, $g = 1$.

achieve a value approximately 8% smaller than amplitudes of forced vibrations for the speed $\varsigma = 3$. At the critical speed $\varsigma_{crit} = 5$, the amplitudes of forced vibrations achieve a value approximately 35% larger than amplitudes obtained for the speed $\varsigma = 6$ (Fig. 10).

The effect of a moving inertial mass in the complex system with elastic $\wp = 0$ and visco-elastic $\wp = \{0.6, 1\}$ inertial interlayer, for the speed $\varsigma = 1$, is presented in Figs. 11–12.
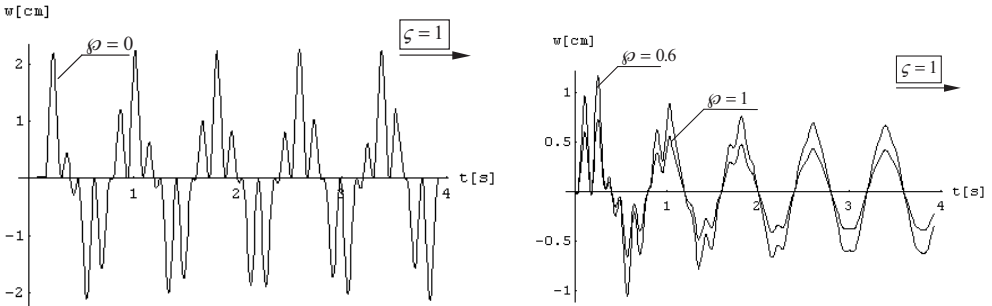

FIG. 11. Forced vibrations of the elastic and visco-elastic complex system for the mass moving with the speeds $\varsigma = 1$ and $\gamma = 0.01$, $\varepsilon = 1$, $\wp = \{0, 0.6, 1\}$, $g = 1$.
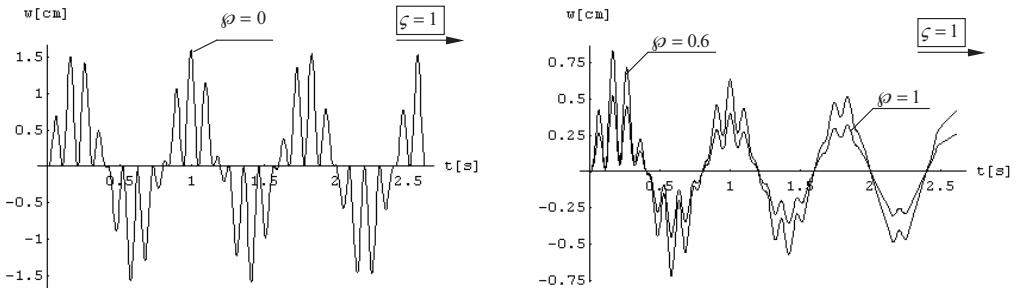

FIG. 12. Forced vibrations of the elastic and visco-elastic complex system for the mass moving with the speeds $\varsigma = 1$ and $\gamma = 1$, $\varepsilon = 0.03$, $\wp = \{0, 0.6, 1\}$, $g = 1$.

In the case when the complex system is loaded by the moving mass for damping coefficients of the visco-elastic interlayer $\wp = \{0.6, 1\}$, the amplitudes of forced vibrations achieve a value approximately 60–90% smaller than amplitudes of forced vibrations for damping coefficient of the elastic interlayer $\wp = 0$ (Figs. 11–12).

The effect of moving mass in the complex system with the elastic and visco-elastic interlayer is presented in Figs. 11, 12 for the various Young moduli of the interlayer $\gamma = 1$ (Fig. 12) and $\gamma = 0.01$ (Fig. 11).

In the case when the complex system with damping is loaded by a moving mass, for the Young modulus of the visco-elastic interlayer $\gamma = 0.01$ (Fig. 11), the amplitudes of forced vibrations achieve a value approximately 12% larger than amplitudes of forced vibrations for the Young modulus of the visco-elastic interlayer $\gamma = 1$ (Fig. 12).

The effect of moving mass in the complex system with the elastic and visco-elastic interlayer is presented in Figs. 11, 12 for various thicknesses of the interlayer $\varepsilon = 1$ (Fig. 11) and $\varepsilon = 0.3$ (Fig. 12). In the case when the complex system with damping is loaded by a moving mass, for a small thickness of the visco-elastic interlayer $\varepsilon = 0.3$ (Fig. 12), the amplitudes of forced vibrations achieve a value approximately 33% smaller than amplitudes of forced vibrations for a large thickness of the visco-elastic interlayer $\varepsilon = 1$ (Fig. 11).

After analysing the results presented in Figs. 11–12 when damping coefficient $\wp = \{0.6, 1\}$ in the interlayer occurs, we conclude that the visco-elastic inertial interlayer can be the vibration damper for the elastic plate which is dynamically loaded by the moving mass and varying in time t. In the case when damping coefficient is equal to zero $\wp = 0$ and in the case when damping coefficient is different from zero $\wp = \{0.6, 1\}$ presented in Figs. 11–12 no resonance occurs in the complex plate with the elastic and visco-elastic inertial interlayers.

4. CONCLUSIONS

- In the case of stationary harmonic loading acting on the compound system, i.e. the platform, the analysis of displacements and the investigations of resonance can be considered in the routine way. The choice of mechanical parameters of the compound system proceeds according to the principles of the classical theory of linear vibrations.

- The problem of vibrations of a compound system excited by the non-stationary inertial, moving load have specific attributes. Therefore the analysis of these vibrations to exceed the general theory of the linear vibrations in the mechanical systems with the time-dependent parameters. It is well-known that a very important quantity of this compound system is the relation between the velocity of moving mass and the so-called critical velocity, that is dependent on the ratio of moving mass to the stationary mass of the mechanical system. In turned out that in the case when the velocity of moving mass small in comparison with the critical high-velocity. Hence it follows that there is no danger to exceed the acceptable displacements in the mechanical system.

References

1. R. Bogacz, R. Szolc, *On non-linear analysis of the geared drive systems by means of the wave method*, Journal of Theoretical and Applied Mechanics, **31**, 2, 393–401, 1993.

2. K. Cabańska–Płaczkiewicz, *Vibrations of the sandwich plate with a viscoelastic inertial interlayer*, The International Journal of Strength of Materials, 103–115, National Academy of Sciences of Ukraine, Institute of Problems of Strength, Kiev 2001.

3. K. Cabańska–Płaczkiewicz, *Vibrations of the complex system with damping under dynamical loading*, The International Journal of Strength of Materials, 2, 82–101, National Academy of Sciences of Ukraine, Institute of Problems of Strength, Kiev 2002.

4. J. Cabański, *Generalized exact method of analysis of free and forced oscillations in the non-conservative physical system*, Journal of Technical Physics, **41**, 4, 471–481, 2000.

5. Kl. Cremer, M. Heckel, E. Ungar, *Structure-Borne Sound, Structural Vibrations and Sound Radiation at Audio Frequencies*, Springer-Verlag, Berlin 1988.

6. R. A. Di Taranto, J. R. Mcgraw, *Vibratory bending of damped laminated plates*, Journal of Engineering for Industry, **91**, 1081–1090, Transactions of the American Society of Mechanical Engineers, 1969.

7. G. Jemielita, *The technical theory of a plate of anaverage thickness*, Journal of Engineering Transactions, 199–220, 1974.

8. G. Kirchhoff, *Über das Gleichgewicht und die Bewegung einer elastichen Scheibe*, Journal fur die Reine und Angewandte Math., **40**, 1, 55–88, 1850.

9. S. Kukla, *Dynamic Green's functions in free vibration analysis of continuous and discrete-continuous mechanical systems*, Pub. of the Częstochowa Univ. of Tech., Częstochowa 1999.

10. W. Kurnik, A. Tylikowski, *Mechanics of laminated elements*, Pub. of the Warsaw Univ. of Tech., Warsaw 1997.

11. R. D. Mindlin, A. Schacknow, H. Deresewicz, *Flexural vibrations of rectangular plates*, Journal of Applied Mechanics, **23**, 3, 430–436, 1956.

12. D. Nashif, D. Jones, J. Henderson, *Vibration damping*, Mir, Moskva 1988.

13. J. Nizioł, J. Snamina, *Free vibration of the discrete-continuous system with damping*, Journal of Theoretical and Applied Mechanics, **28**, 1–2, 149–160, 1990.

14. W. Nowacki, *The Building Dynamics*, Warsaw, Arkady 1972.

15. Z. Oniszczuk, *Free vibrations of elastically connected rectangular double-plate compound system*, Building Engineering, Pub. of the Warsaw Univ. of Tech., 132, 183–109, Warsaw 1998.

16. Z. Oniszczuk, *Vibration analysis of the compound continuous systems with elastic constraints*, Pub. of the Rzeszow Univ. of Tech., Rzeszów 1997.

17. Z. Osiński, *Damping of the mechanical vibration*, PWN, Warsaw 1979.

18. J. Osiowski, *A draft of the operator calculus*, Warsaw: WNT, 1981.

19. N. D. Pankratova, B. Nikolaev, E. Świtoński, *Nonaxisymmetrical deformation of flexible rotational shells in classical and improved statement*, Journal of Engineering Mechanics, **3**, 2, 89–96, 1996.

20. N. D. PANKRATOVA, A. A. MUKOED, *Deformation of the thick laminated orthotropic plate*, XXXIV Symposium of Model. in Mech., Silesian Univ. of Tech., 122, 251–256, Gliwice 1995.

21. E. REISSNER, *On transverse bending of plates, including the effect of transverse shear deformation*, Int. Journal of Solid Structures, **11**, 569–573, 1975.

22. M. RENAUDOT, *Etude de l'influence des charges en mouvement sur la resistance des ponts metallique*, Annales des Ponts et Chausses, **1**, 145–204, 1861.

23. Cz. RYMARZ, *Mechanics of continua*, PWN, Warsaw 1993.

24. W. SZCZEŚNIAK, *The problems of vibrations of dynamical plates under moving inertial loads*, Building Engineering, Pub. of the Warsaw Univ. of Tech., **119**, 1–112, Warsaw 1992.

25. W. SZCZEŚNIAK, *Vibrations of plates. Theoretical fundamentals of the mechanics of track-airfield structure*, Research Institute of Track and Bridges, Warsaw 2000.

26. S. P. TIMOSHENKO, S. WOINOWSKY-KRYGIER, *Theory of plates and shells*, Arkady, New York, Toronto, London 1956.

27. F. TSE, I. MORSE, R. HINKLE, *Mechanical vibrations theory and applications*, Allyn and Bacon, Boston 1978.

28. A. TYLIKOWSKI, *Influence of bonding layer on piezoelectric actuators of an axisymmetrical annular plate*, Journal of Theoretical and Applied Mechanics, **38**, 3, 607–621, 2000.

29. T. M. WANG, *Natural frequencies of continuous Timoshenko beams*, Journal of Sound and Vibration, **13**, 409–414, 1970.

30. E. WINKLER, *Die Lehre von der Elastizität und Festigkeit, Dominicus*, Prag 1867.

31. M. WOŹNIAK, *Railway embankment as the building foundation*, Mathematical Modelling, Scientific Treatises and Monograhs, SGGW-AR, Warsaw 1991.

NORMAL PENETRATION OF THE RIGID PENETRATOR INTO ELASTIC-PLASTIC HALF-SPACE WITH VISCOSITY

E. W ł o d a r c z y k

Military University of Technology
Faculty of Mechatronic

S. Kaliskiego 2, 00-908 Warszawa, Poland

The analytical closed-form solution of the normal penetration problem of a rigid core (penetrator) of a jacket-bullet into elastic-plastic half-space (thick target) is presented in this paper. The cohesive resistance of the target, frictional effects, and acceleration of the target material in the neghbourhood of the penetrator (virtual mass effect) is taken into consideration. On the basis of the derived closed analytical formulae, influence of these parameters on the penetration depth may be investigated. Among other things, it appears from calculations that the boundary penetration depth is intensivly reduced by the force of viscous friction.

Moreover, the mean value of the coefficient of viscous friction (μ) for a given penetrator-target system may be determined. For this purpose it is necessary to define experimentally the penetration depth h_k at a given impact velocity.

Key words: terminal ballistics, normal penetration, jacket-bullet, rigid penetrator.

1. Introduction

A penetration of projectiles into various targets has been a vast field of theoretical and experimental investigations for many scientists. Wide reviews of the literature concerning this question have been presented in the papers [1, 2].

It is well known that one of the principal parameters which bounds the penetration depth of projectile into a target, is the impact velocity. The impact velocity values of small arms projectiles are contained within the interval $100 \div 1000$ m/s. In this interval of the impact velocity, the ogival penetrator, made of a sintered carbide or of the special-purpose steel, keeps primary shape during of the penetration into the soft metal target. This fact is shown in Fig. 1. The braked undeformed core, and the pulled-off core and pressed jacket of the bullet is depicted in this figure. In these cases, the penetrator (core) can be approximated by a rigid body.

It results from the scientific literature that axial resisting force of the target, acting on a unit of the penetrator cross-section, is defined by the following formula [1, 2]:

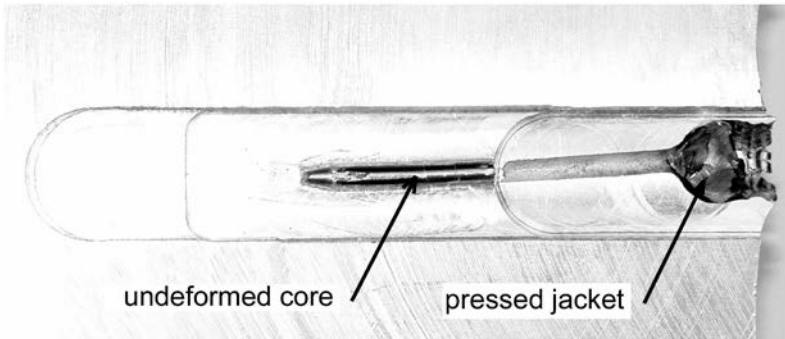$$(1.1) \qquad \sigma = c + bv + av^2.$$

FIG. 1. The braked core (sintered carbide) of the jacket bullet (calibre: 7.62 mm) in the duralumin (PA6) target. Impact velocity $V = 812$ m/s.

The terms on the right-hand side of Eq. (1.1) are associated with the cohesive resistance of the target, frictional effects, and the acceleration of target material in the neighbourhood of the projectile (virtual mass effect), respectively.

The problem of penetration of the rigid projectile into a metal target without the second term of the formula (1.1) was considered [1–5]. Analytical solution of this problem for complete formula (1.1), and analysis of the dependence of the penetration depth on the respective terms of the formula (1.1) have been presented in this paper.

2. FORMULATION OF THE PROBLEM

We assume that a rigid core of the jacket bullet is a penetrator. The jacket is separated from the core during embedding of the projectile into a target. Subsequently the free core penetrates the target, as a rigid penetrator.

Normal penetration of the rigid penetrator into metallic semi-infinite space (thick target) is considered in this paper. The penetrator has rotational symmetry. Direction of the penetrator velocity overlaps its axis and is perpendicular to the plane of the semi-infinite space. On the penetrator acts a unit axial resisting force of the target, which is defined by the formula (1.1).

Under these assumptions, the penetrator's motion into metal target can be described by the following differential equation:

$$(2.1) \qquad \rho_p L \frac{dv}{dt} = -\left(av^2 + bv + c\right),$$

and by the initial condition

$$(2.2) \qquad v(0) = V,$$

where symbols L, ρ_p and V stand for the penetrator length, density of the penetrator material and impact velocity, respectively.

According to the data given in [3–5], the coefficients a and c can be described by the following expressions:

$$(2.3) \qquad a = k\rho_t, \qquad c = H_t,$$

where symbols H_t, ρ_t and k denote the dynamic hardness of the target material, density of the target material and coefficient of the nose shape of the penetrator, respectively. The value of the coefficient k can be estimated by means of the formula [6, 7]:

$$(2.4) \qquad k = 1 - \frac{1}{8}\left(\frac{D}{R}\right)^2,$$

where symbols D and R stand for diameter of the greatest cross-section of the penetrator and the radius of a sphere which approximates the contact space of the penetrator nose with crater bottom, respectively.

The symbol b denotes the coefficient of the mean absolute viscosity.

We introduce the following dimensionless quantity:

$$(2.5) \qquad \mu = \frac{b}{\rho_t V}.$$

The quantity μ is termed as the mean coefficient of a viscous friction.

3. Solution of the problem

On separating the variables v and t in Eq. (2.1) and integrating, we obtain:

$$(3.1) \qquad \int \frac{dv}{av^2 + bv + c} = -\frac{t}{\rho_p L} + C,$$

where an integration constant C is defined by the initial condition (2.2).

The left-hand side of Eq. (3.1) can be expressed by the following functions:

$$(3.2) \qquad \frac{1}{\sqrt{\Delta}}\ln\left|\frac{2av + b - \sqrt{\Delta}}{2av + b + \sqrt{\Delta}}\right| \qquad \text{for} \quad b^2 > 4ac,$$

$$(3.3) \qquad \frac{2}{\sqrt{-\Delta}}\operatorname{arc\,tg}\frac{2av + b}{\sqrt{-\Delta}} \qquad \text{for} \quad b^2 < 4ac,$$

$$(3.4) \qquad -\frac{2}{2av + b} \qquad \text{for} \quad b^2 = 4ac,$$

where

$$(3.5) \qquad \Delta = b^2 - 4ac.$$

It results from the above relationships that the considered problem has three different solutions, which are determined by relations between terms b^2 and $4ac$.

3.1. Solution of the problem for large absolute viscosity, i.e.:
$$b^2 > 4ac \text{ or } \mu^2 > (4kH_t/\rho_t V^2) = \mu_0^2$$

From expressions (3.1) and (3.2), as well as the initial condition (2.2), after simple transformation, we obtain:

$$(3.6) \qquad \bar{v}(\eta) = \frac{\mu}{2k}\left[(1+c_1)\frac{\exp(-a_1\eta)}{b_1 - \exp(-a_1\eta)} - (1-c_1)\frac{b_1}{b_1 - \exp(-a_1\eta)}\right],$$

where:

$$\eta = \frac{Vt}{L}, \qquad \bar{v} = \frac{v}{V}, \qquad \mu = \frac{b}{\rho_t V}, \qquad a_1 = \mu c_1 \frac{\rho_t}{\rho_p},$$

(3.7)

$$b_1 = \frac{2k + \mu(1+c_1)}{2k + \mu(1-c_1)}, \qquad c_1 = \sqrt{1 - 4k\frac{H_t}{\mu^2\rho_t V^2}} = \sqrt{1 - \left(\frac{\mu_0}{\mu}\right)^2}.$$

It follows from Eq. (3.6) that the penetrator is completely braked ($v = 0$) after time $t_k = (L/V)\eta_k$, where

$$(3.8) \qquad\qquad\qquad \eta_k = \frac{1}{a_1}\ln\frac{1+c_1}{(1-c_1)b_1}.$$

The current penetration depth of the penetrator into the target is defined by the following integral:

$$(3.9) \qquad\qquad\qquad l(t) = \int\limits_0^t v(\tau)d\tau.$$

On substituting the relation (3.6) into Eq. (3.9) and integrating, we obtain:

$$(3.10) \qquad h(\eta) = \frac{\mu}{2k}\left[\frac{2c_1}{a_1}\ln\frac{b_1 - \exp(-a_1\eta)}{b_1 - 1} - (1-c_1)\eta\right],$$

where

$$h = \frac{l}{L}.$$

The boundary (maximal) penetration depth of the penetrator into the target is defined by the formula:

$$(3.11) \qquad h_k = h(\eta_k) = \frac{\mu}{2k}\left[\frac{2c_1}{a_1}\ln\frac{b_1 - \exp(-a_1\eta_k)}{b_1 - 1} - (1-c_1)\eta_k\right].$$

3.2. Solution of the problem for small viscosity, i.e.:
$$b^2 < 4ac \text{ or } \mu^2 < (4kH_t/\rho_t V^2) = \mu_0^2$$

In this case, from expressions (3.1) and (3.3), as well as (2.2) we get:

(3.12)
$$\bar{v}(\eta) = \frac{1}{2k}\left[c_2 \operatorname{tg}\left(\operatorname{arc tg}\frac{2k+\mu}{c_2} - \frac{c_2}{2}\frac{\rho_t}{\rho_p}\eta\right) - \mu\right],$$

(3.13)
$$\eta_k = \frac{2}{c_2}\frac{\rho_p}{\rho_t}\left(\operatorname{arc tg}\frac{2k+\mu}{c_2} - \operatorname{arc tg}\frac{\mu}{c_2}\right),$$

where
$$c_2 = \sqrt{4k\frac{H_t}{\rho_t V^2} - \mu^2} = \sqrt{\mu_0^2 - \mu^2}.$$

Substituting relationship (3.12) into Eq. (3.9) and integrating, we have:

(3.14)
$$h(\eta) = \frac{1}{k}\frac{\rho_p}{\rho_t}\left[\ln\left|\frac{\cos\alpha\,(\eta)}{\cos\alpha_0}\right| - \frac{\mu}{2}\frac{\rho_t}{\rho_p}\eta\right],$$

where

(3.15)
$$\alpha(\eta) = \operatorname{arc tg}\frac{2k+\mu}{c_2} - \frac{c_2}{2}\frac{\rho_t}{\rho_p}\eta,$$
$$\alpha_0 = \operatorname{arc tg}\frac{2k+\mu}{c_2}.$$

The boundary penetration depth is defined in this case by the formula:

(3.16)
$$h_k = h(\eta_k) = \frac{1}{k}\frac{\rho_p}{\rho_t}\left[\ln\left|\frac{\cos\alpha\,(\eta_k)}{\cos\alpha_0}\right| - \frac{\mu}{2}\frac{\rho_t}{\rho_p}\eta_k\right],$$

where

(3.17)
$$\alpha(\eta_k) = \operatorname{arc tg}\frac{2k+\mu}{c_2} - \frac{c_2}{2}\frac{\rho_t}{\rho_p}\eta_k = \operatorname{arc tg}\frac{\mu}{c_2}.$$

It results from formulae (3.15) and (3.17) that for $\mu = 0$ [lack of the viscosity term in the expression (1.1)], there are:

(3.18)
$$\alpha_0 = \operatorname{arc tg}\frac{2k}{\sqrt{4kH_t/\rho_t V^2}} = \sqrt{k\frac{\rho_t V^2}{H_t}},$$
$$\alpha\,(\eta_k) = 0.$$

Substituting the formulae (3.18) into the relation (3.16) and taking into consideration the following trigonometric identity:

$$\arctg x = \arccos\left(1/\sqrt{1+x^2}\right),$$

we get:

(3.19)
$$h_k = \frac{1}{2k}\frac{\rho_p}{\rho_t}\ln\left(1 + k\frac{\rho_t V^2}{H_t}\right).$$

Such expression has been derived in papers [3–5].

3.3. Singular solution: $b^2 = 4ac$ or $\mu^2 = \mu_0^2 = 4kH_t/\rho_t V^2$

In accordance with the formulae (3.1), (3.4) and (2.2) we obtain:

(3.20)
$$\bar{v}(\eta) = \frac{1}{2k}\left[\frac{2(2k+\mu_0)}{2+(\rho_t/\rho_p)(2k+\mu_0)\eta} - \mu_0\right].$$

In this case, the penetrator is completely braked on the lapsing of time

(3.21)
$$\eta_k = \frac{Vt_k}{L} = \frac{4k}{\mu_0(\rho_t/\rho_p)(2k+\mu_0)}.$$

After substitution of the relationship (3.20) into integral (3.9) and integrating, we have:

(3.22)
$$h(\eta) = \frac{l(\eta)}{L} = \frac{1}{k}\frac{\rho_p}{\rho_t}\left[\ln\left(1 + \frac{2k+\mu_0}{2\rho_p/\rho_t}\eta\right) - \frac{\mu_0}{2\rho_p/\rho_t}\eta\right].$$

The boundary penetration depth in this case is:

(3.23)
$$h_k = h(\eta_k) = \frac{1}{k}\frac{\rho_p}{\rho_t}\left[\ln\left(1 + \frac{2k}{\mu_0}\right) - \frac{2k}{2k+\mu_0}\right].$$

Thus, we obtain the analytical solution of the examined problem for each of the mean values of the viscous friction coefficient μ.

4. PRELIMINARY ANALYSIS OF THE BOUNDARY PENETRATION DEPTH

It follows from the above derived formulae, that normal penetration depth of the core of the jacket projectile into metal half-space depends on the following parameters: dynamic hardness and density of target metal (H_t, ρ_t), impact velocity (V), unit mass of the penetrator ($\rho_p L$), nose shape of the penetrator (k), and the mean coefficient of the viscous friction (μ).

The preliminary analysis of the boundary penetration depth h_k has been made for the following materials:

penetrator: sintered metal (WHA), $\rho_p = 17200$ kg/m^3;

target: 1. Ingot iron, $\rho = 7850$ kg/m^3, $H_t = 1638$ MPa;
         2. Aluminium, $\rho = 2700$ kg/m^3, $H_t = 260$ MPa;
         3. Duralumin, $\rho = 2800$ kg/m^3, $H_t = 1300$ MPa.

Two values of the coefficient k were assumed, namely:

$k = 0.5$ – hemispherical – ended projectile,

$k = 1.0$ – flat – ended projectile.

Some calculation results are depicted in Figs. 2–5. It seems that the qualitative variations of the boundary penetration depth h_k versus coefficient μ are similar for various materials of the target. On the contrary, significant quantitative differences occur among curves $h_k(\mu)$ plotted for targets made from various metals. These variations are visible in the Figs. 2–5. For example, the boundary penetration depth into aluminium target is about five times greater (at $\mu \approx 0$) than into the duralumin one (Fig. 5). This difference decreases when the coefficient μ increases.

The penetration depth is intensively reduced by increase of the coefficient μ. The highest gradient decreasing of the penetration depth occurs in the initial increase stage of the coefficient μ. The viscous friction decreases the penetration depth several times in comparison with the frictionless penetration.
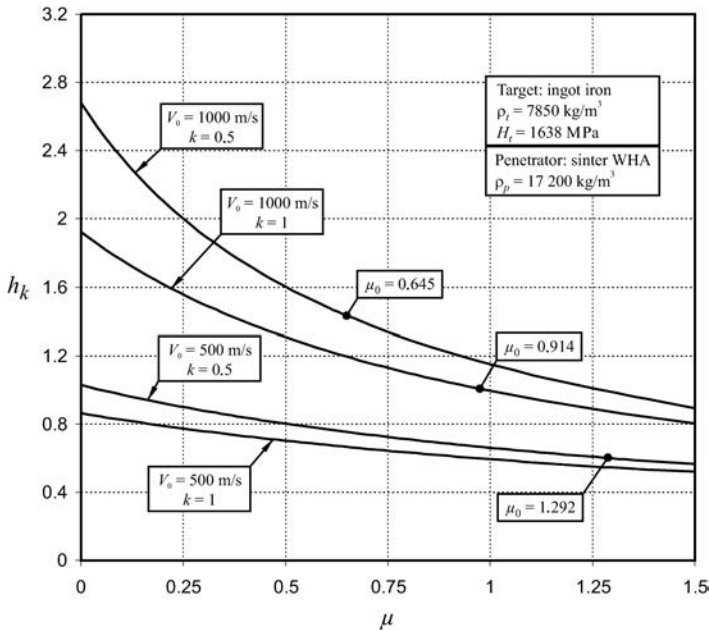

FIG. 2. Variation of quantity h_k as a function of coefficient μ.
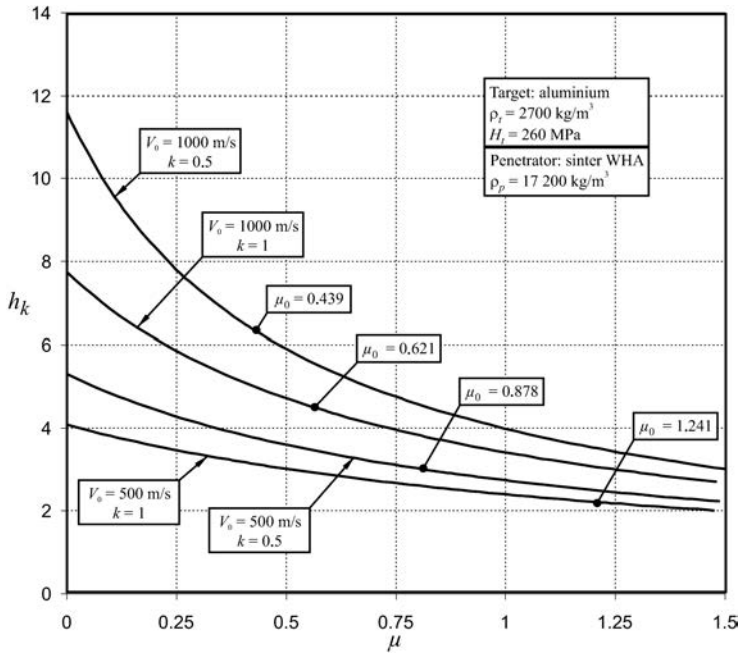
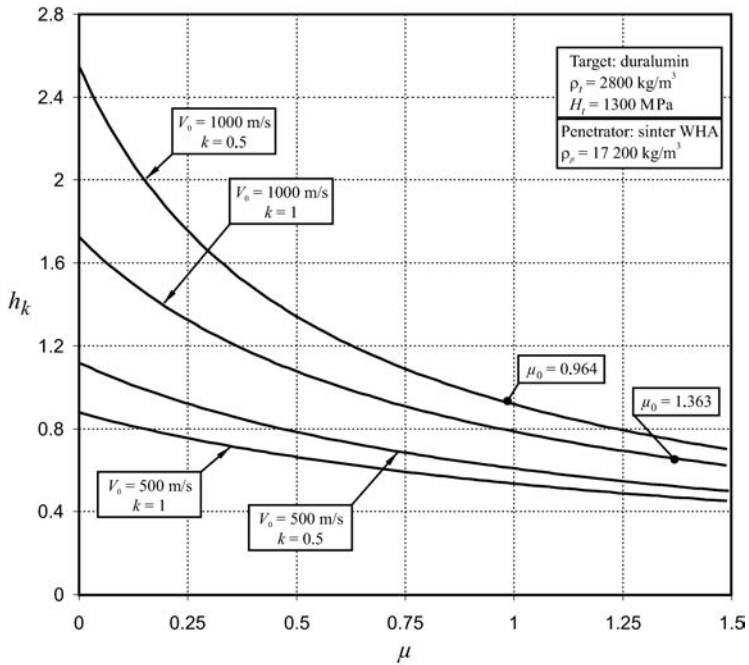FIG. 3. Variation of quantity h_k as a function of coefficient μ.

FIG. 4. Variation of quantity h_k as a function of coefficient μ.
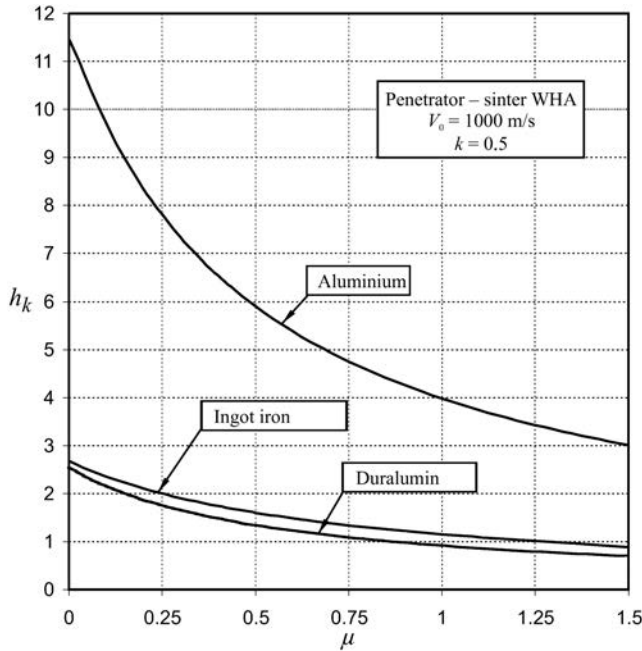
FIG. 5. Variation of quantity h_k as a function of coefficient μ for the three target-penetrator systems.

Let us observe conclusion that for a given penetrator-target system, the mean value of the coefficient μ may be defined by means of the formulae (3.11) or (3.16). For this purpose it is necessary to define experimentally the quantity h_k at the given impact velocity and then the mean value of the coefficient μ can be determined.

5. CONCLUSIONS

The analytical model of normal penetration of the rigid penetrator into the thick metal target has been presented in this paper. In this model, cohesive resistance of the target, frictional effects, and the acceleration of target material in the neighbourhood of the penetrator (virtual mass effect), have been taken into consideration. On the basis of the derived closed analytical solution, the influence of the respective terms of the formulae (1.1) on the penetration depth is investigated.

It is found that the penetration depth is intensively reduced by the forces of viscous friction. By means of this model, the mean value of the coefficient of viscous friction (μ) for a given penetrator-target system may be also determined.

Preliminary experimental investigations support the usefulness of the presented theoretical model in the calculations of the terminal ballistics.

References

1. M. E. BACKMAN, W. GOLDSMITH, *The mechanics of penetration of projectiles into targets*, Int. J. Engng Sci., **16**, 1, 1–99 1978.

2. W. GOLDSMITH, *Review. Non-ideal projectile impact on targets*. Int. J. Impact Engng, **22**, 23, 95–395, 1999.

3. J. S. RINEHART, J. PEARSON, *Behavior of metals under impulsive loads*, ASM, Cleveland, Ohio 1954.

4. F. F. VITMAN, N. A. ZLATIN, *On process of a collision of the deformable bodies and its modeling. II. State and problem theory* [in Russian], Zh.T.F., **33**, 8, 1963.

5. E. WŁODARCZYK, Z. GŁODOWSKI, M. MICHAŁOWSKI, *Penetration of undeformable projectile in metallic half-space* [in Polish], Biul. WAT, **51**, 10, 33–45, 2002.

6. C. CRANZ, Lehrbuch der Ballistik, Berlin – Springer, 1925–1927.

7. L. V. BIELYAKOV, F. F. VITMAN, N. A. ZLATIN, *On process of a collision of the deformable bodies and its modeling. III – On similarity of current values of parameters of true and modeling processes* [in Russian], Zh.T.F., **34**, 3, 1964.